ISPRS Journal of Photogrammetry and Remote Sensing 215 (2024) 419–441

Contents lists available at ScienceDirect

ISPRS Journal of Photogrammetry and Remote Sensing

journal homepage: www.elsevier.com/locate/isprsjprs

Towards a gapless 1 km fractional snow cover via a data fusion framework

Xiongxin Xiao [a,b], Tao He [a,*], Shuang Liang [c], Shunlin Liang [d], Xinyan Liu [a], Yichuan Ma [a], Jun Wan [e]

[a] Hubei Key Laboratory of Quantitative Remote Sensing of Land and Atmosphere, School of Remote Sensing and Information Engineering, Wuhan University, Wuhan 430079, China
[b] Institute of Geography, Oeschger Center for Climate Change Research, University of Bern, Hallerstrasse 12, 3012 Bern, Switzerland
[c] Aerospace Information Research Institute, Chinese Academy of Sciences, Beijing 100094, China
[d] Department of Geography, University of Hong Kong, Hong Kong 999077, China
[e] Wuhan Regional Climate Center, China Meteorological Administration, Wuhan 430010, China

ARTICLE INFO

Keywords:
Fractional snow cover
Data fusion
North America
MODIS
Passive microwave

ABSTRACT

Accurate quantification of snow cover facilitates the prediction of snowmelt runoff, the assessment of freshwater availability, and the analysis of Earth's energy balance. Existing fractional snow cover (FSC) data, however, often suffer from limitations such as spatial and temporal gaps, compromised accuracy, and coarse spatial resolution. These limitations significantly hinder the ability to monitor snow cover dynamics effectively. To address these formidable challenges, this study introduces a novel data fusion framework specifically designed to generate high-resolution (1 km) daily FSC estimation across vast regions like North America, regardless of weather conditions. It achieved this by effectively integrating the complementary spatiotemporal characteristics of both coarse- and fine-resolution FSC data through a multi-stage processing pipeline. This pipeline incorporates innovative strategies for bias correction, gap filling, and consideration of dynamic characteristics of snow cover, ultimately leading to high accuracy and high spatiotemporal completeness in the fused FSC data. The accuracy of the fused FSC data was thoroughly evaluated over the study period (September 2015 to May 2016), demonstrating excellent consistency with independent datasets, including Landsat-derived FSC (total 24 scenes; RMSE=6.8–18.9 %) and ground-based snow observations (14,350 stations). Notably, the fused data outperforms the widely used Interactive Multi-sensor Snow and Ice Mapping System (IMS) daily snow cover extent data in overall accuracy (0.92 vs. 0.91), F1_score (0.86 vs. 0.83), and Kappa coefficient (0.80 vs. 0.77). Furthermore, the fused FSC data exhibits superior performance in accurately capturing the intricate daily snow cover dynamics compared to IMS data, as confirmed by superior agreement with ground-based observations in four snow-cover phenology metrics. In conclusion, the proposed data fusion framework offers a significant advancement in snow cover monitoring by generating high-accuracy, spatiotemporally complete daily FSC maps that effectively capture the spatial and temporal variability of snow cover. These FSC datasets hold substantial value for climate projections, hydrological studies, and water management at both global and regional scales.

1. Introduction

Accurate and repeated observations of snow cover are of utmost importance for effective water resource management and reliable climatic forecasting (Lettenmaier et al., 2015; Li et al., 2022; Qin et al., 2020; Rittger et al., 2016; Shugar et al., 2021; Xiao et al., 2020). The snowpack, as a vital reservoir of solid water, plays a critical role in maintaining a balanced water supply for ecosystems and human society (Barnett et al., 2005; Sturm, 2015). However, this delicate balance is susceptible to disruptions arising from alterations in snow proportion and snowmelt timing (Berghuijs et al., 2014). Seasonal snow cover anomalies stand as one of the most prominent and unmistakable consequences of global climate change, with far-reaching implications for various sectors, particularly in basins heavily dependent on snowmelt runoff, such as irrigated agriculture and food production (Musselman et al., 2021; Qin et al., 2020). Amidst the backdrop of escalating water demand and the occurrence of extremely high temperatures, accurate forecasting of snowmelt runoff has become more crucial than ever. The

* Corresponding author.
E-mail address: taohers@whu.edu.cn (T. He).

https://doi.org/10.1016/j.isprsjprs.2024.07.018
Received 2 February 2024; Received in revised form 14 July 2024; Accepted 19 July 2024
Available online 29 July 2024

recent drought conditions in western North America have further highlighted the urgent demand to develop innovative approaches that ensure continuous and accurate observations of snow cover under all weather conditions (Hedrick et al., 2018).

Station observations and *in-situ* measurements have traditionally been the primary methods for acquiring snowpack information. However, advanced remote sensing techniques have transformed satellite remote sensing into a powerful alternative for providing large-scale spatial snow cover observations (Dietz et al., 2012; Xiao et al., 2018). Optical satellite sensors, including the Landsat series (Dozier, 1989; Girona-Mata et al., 2019), Sentinel-2 series (Gascoin et al., 2019), Moderate Resolution Imaging Spectroradiometer (MODIS) (Kuter et al., 2018; Painter et al., 2009), Visible Infrared Imaging Radiometer Suite (VIIRS) (Riggs et al., 2017; Rittger et al., 2020a), and Advanced Very High Resolution Radiometer (AVHRR) (Hao et al., 2021; Zhou et al., 2013), have been extensively used to monitor snow cover since the mid-60 s and remain the primary data source for snow cover mapping (Gafurov and Bárdossy, 2009). However, these optical satellite sensors often lack snow cover information under overcast and dark conditions, particularly in polar regions, restricting their ability to provide year-round snow cover observations. Several approaches have been proposed to address this limitation for cloud removal and data gap filling in optical-based snow cover area products (e.g., Dozier et al., 2008; Huang et al., 2018; Jing et al., 2022; Xing et al., 2022). For instance, Dozier et al. (2008) introduced the space–time cube method to fill fractional snow cover (FSC) product gaps by incorporating temporal and spatial information and applying a set of rules to exclude clouds from MODIS snow cover data (Gafurov and Bárdossy, 2009; López-Moreno et al., 2020). Another approach, the Hidden Markov random field (HMRF) algorithm, has been developed to generate a cloud-free binary snow map in basins (Huang et al., 2018). To obtain cloud-free FSC area data, Wang et al. (2018) successfully replaced cloud pixels in the MODIS snow cover data with FSC values from the geostationary satellite data and employed a temporal interpolation method to handle any remaining cloudy pixels. Aside from binary and fractional snow cover, Jing et al. (2022) employed a spatiotemporal adaptive fusion method with an error correction approach to produce cloud free MODIS Normalized Difference Snow Index (NDSI) data, a commonly used measure of snow cover distribution. Additionally, Rittger et al. (2021) developed a downscaling method that enhances the spatiotemporal resolution (daily, 30 m) for estimating snow cover area by combining Landsat data and MODIS product. Similarly, previous work has also employed the Enhanced Spatial and Temporal Adaptive Reflectance Fusion Model (ESTARFM) method to fuse clear-sky NDSI data from MODIS-Landsat or Landsat-Sentinel image pairs, achieving higher spatial resolution (Bousbaa et al., 2022; Gao et al., 2022).

In contrast to optical data, passive microwave (PM) data offer a distinct advantage in detecting large-scale snow cover distribution under all weather conditions due to their lower atmospheric interference. Microwave signals exhibit a heightened sensitivity to variations in snow cover properties, enabling the retrieval of specific snow characteristics using coarse-resolution PM brightness temperature data (Dietz et al., 2012). Several studies have utilized this data to generate binary snow cover maps (Grody and Basist, 1996; Liu et al., 2018; Xiao et al., 2018). However, only a limited number of investigations have explored the estimation of FSC from PM brightness temperature data (Xiao et al., 2022a, 2021). Employing PM brightness temperature data to determine snow cover areas poses substantial challenges and uncertainties. For example, PM brightness temperature data may fail to detect thin or patchy snow cover and misclassify non-snow scatterers like precipitation, frozen ground, and cold desert areas (Foster et al., 2011; Grody and Basist, 1996; Xiao et al., 2022a). Additionally, the coarse spatial resolution of PM brightness temperature data restricts the applicability of their derived products to regional or local-scale assessments.

To overcome the limitations of single-sensor data and provide fine-resolution, spatially complete snow cover information in near real-time, a collaborative data fusion approach becomes indispensable. Numerous studies have successfully retrieved snow cover properties by leveraging complementary information from optical and passive microwave sensors, highlighting the advantages of multi-sensor synergy for snow cover mapping (Bergeron et al., 2014; Foster et al., 2011; Gao et al., 2010; Romanov, 2017; Romanov et al., 2000). When cloud-free optical images are available, researchers generally favor optical data-derived products due to their superior spatial resolution, which instills greater confidence in snow cover identification (Gao et al., 2010; Yang et al., 2014). Hence, a common fusion method utilizes optical-based snow cover information under clear-sky conditions and supplements it with PM-based data during cloudy or dark periods (Foster et al., 2011; Huang et al., 2016; Liang et al., 2008). For instance, geostationary optical satellite data can be integrated with polar-orbiting microwave satellite data for snow cover monitoring (Yang et al., 2014). PM-based snow depth products can also be converted to binary snow cover and used to fill the remaining gap pixels after applying a spatiotemporal model (Hao et al., 2021). Deng et al. (2015) employed AMSR-E snow water equivalent products to classify cloudy pixels as snow or snow-free when mapping cloud-free FSC. These approaches undoubtedly expand the snow-covered area depicted on the blended binary map.

While numerous studies have explored the integration of optical and PM data for snow cover estimation, practical implementations in FSC estimation of such fusion methods remain limited. This study focuses on developing a novel data fusion framework for producing daily and spatially complete FSC data at a 1 km resolution for the North American region. The proposed framework leverages the complementary spatiotemporal characteristics of both coarse- and fine-resolution FSC data. To demonstrate the practical performance of the framework in FSC estimation, we employed coarse-resolution and fine-resolution FSC datasets from our previous works (Xiao et al., 2022a, 2022b). Section 2 provides an overview of these datasets, details on the Landsat data, ground snow measurements for validation, and the Interactive Multi-sensor Snow and Ice Mapping System (IMS) used for comparison. Section 3 delves into the processes involved in the proposed data fusion framework, including the employed pipelines and evaluation measures used for FSC estimations assessment. Section 4 presents a comprehensive analysis of the evaluation results, highlighting the effectiveness of the proposed framework. Section 5 discusses the uncertainties and limitations inherent to the data fusion framework and its estimations of fused FSC.

2. Datasets

Table 1 provides a comprehensive overview of the datasets employed in this study, including two primary sources of FSC data (derived from optical and PM satellite imagery), land cover types, Landsat-derived snow cover data, two types of ground observations for validation purposes, and the Interactive Multi-sensor Snow and Ice Mapping System (IMS) data for comparative analysis of the fused FSC results.

Table 1
Multisource data for input, validation, and comparison during the period from September 2015 to May 2016.

Sources	Data name	Spatial/ temporal resolution	Variable
Input data	Passive microwave data-based FSC (PM_FSC)	6.25 km/daily	FSC
	Optical data-based FSC (MODIS_FSC)	500 m/daily	
Auxiliary	MCD12Q1	500 m/yearly	Land cover types
Validation	14,350 ground sites	Point/daily	Snow depth
	3000 ground sites		
	Landsat 8 (OLI) based FSC	30 *m*	FSC
Comparison	IMS	1 km	Snow cover extent

2.1. Coarse- and fine-resolution FSC data pairs

2.1.1. Coarse-resolution FSC data: Passive microwave data-based FSC

The coarse-resolution PM-based FSC data were derived from daily PM brightness temperature data at three frequencies (19-, 37-, and 91-GHz) for both horizontal and vertical polarization, enabling effective capture of surface snow cover information under all weather conditions (Xiao et al., 2022a). The PM brightness temperature data, provided at an enhanced resolution by the National Snow and Ice Data Center (NSIDC) (Brodzik et al., 2016), are accessible through the website https://nsidc.org/data/NSIDC-0630/versions/1.

Savoie et al. (2009) noted that atmospheric effects can lead to an underestimation of approximately 17 % in the snow cover area, particularly when using high-frequency channels. Further, microwave radiation can be influenced by complex terrain (Li et al., 2014) and forest cover (Guglielmetti et al., 2007; Roy et al., 2012). To address these challenges, we employed a radiative transfer model to isolate snowpack signatures in satellite-observed brightness temperature, thereby mitigating the impacts of the atmosphere, topography, and forests. Subsequently, a machine learning method was utilized to develop an FSC retrieval model based on the processed PM brightness temperature data for North America. This model incorporated variations in soil properties (moisture and temperature), land cover types, vegetation coverage, geographical location, and additional snow-related variables to minimize uncertainties in FSC estimations (Xiao et al., 2022a). The resulting PM-based FSC estimation product, referred to as PM_FSC, has a resolution of 6.25 km and has undergone error reduction in non-snow scatters. For more details, please refer to Xiao et al. (2022a).

2.1.2. Fine-resolution FSC data: Optical data-based FSC

In contrast to PM data, optical remote sensing images provide high-resolution data for monitoring surface snow cover distribution. Previous studies have shown that the standard MODIS FSC estimation algorithm, based on snow cover products (MY/OD10A1), generally performs better over non-vegetated areas but exhibits significant discrepancies in forested areas (Hall and Riggs, 2007; Maurer et al., 2003; Parajka et al., 2012). Snow cover in forested regions is consistently underestimated, especially in dense forests and at high viewing angles (Rittger et al., 2020b; Xin et al., 2012). To address this shortcoming, Xiao et al. (2022b) developed an integrated FSC retrieval model based on the Extremely Randomized Trees method, which enhances FSC estimation in vegetation-covered areas using MODIS seven-band surface reflectance data (500 m) and additional auxiliary data. This FSC inversion model considerably reduces estimation errors and uncertainties associated with varying viewing geometries and vegetation cover, generating FSC products at 500 m spatial resolution over Norther America (referred to as MODIS_FSC). The effectiveness of canopy adjustment in characterizing ground-level snow distribution has been demonstrated. However, it is crucial to recognize that canopy adjustment requires further validation and development of a robust function through additional *in-situ* measurements and fine-resolution observations (Liu et al., 2008; Raleigh et al., 2013; Rittger et al., 2020b; Xiao et al., 2022b). Consequently, this analysis excludes MODIS_FSC estimations with significant errors and uncertainties (i.e., pixel viewing angle exceeding 60°).

2.2. Ground snow depth observations

Although there is limited spatial representation of ground-based snow observations in coarse-spatial resolution imagery, *in-situ* observations remain the most authentic and reliable standard for validating snow cover detection. This study gathered *in-situ* snow depth observations from 14,350 sites compiled by the Global Historical Climatology Network-Daily, Version 3 (Menne et al., 2012) (https://www.nce-i.noaa.gov/access/metadata/landingpage-/bin/iso?id = gov.noaa.ncdc:C00861).

A comprehensive collection of snow depth observations from 14,350 sites was used to evaluate the snow cover mapping capability of various snow cover area datasets. To specifically assess the accuracy of daily continuous snow dynamics, a subset of approximately 3,000 sites was selected from the initial set of 14,350 sites, ensuring they possessed complete daily measurement records from September 2015 to May 2016. This subset was chosen to capture daily dynamic characteristics of snow cover over time. Notably, during the study period, 12,083 out of 14,350 sites in the initial collection and 2,578 out of 3,000 sites in the selected subset showed snow records (snow depth > 0 cm). This observation highlights that a substantial portion of the stations recorded snowfall during the study period. The presence of snow at these sites reinforces the credibility and relevance of the validation process for our study's objectives.

2.3. Landsat OLI images

This study used Landsat images as reference snow cover observations to assess the fused FSC estimations. Carefully selected 24 scenes of Landsat 8 Level 1 T land surface reflectance data acquired during the study period from September 2015 to May 2016 (Fig. 1 right) were obtained from the United States Geological Survey (USGS). These scenes underwent a comprehensive screening procedure to ensure minimal cloud cover (<1%) and extensive fractional snow coverage over large areas, adhering to established guidelines (Kuter et al., 2018; Wulder et al., 2012; Xiao et al., 2022b). Landsat images were visually inspected individually to exclude those with substantial areas of cloud cover or snow-free conditions. Table A of the Appendix provides comprehensive information about these 24 Landsat scenes. Binary snow cover maps (30 m) were generated using the SNOWMAP algorithm (Hall et al., 1995), while a cloud mask was produced using the Fmask algorithm (Qiu et al., 2019). Subsequently, by averaging the snow pixel counts within a 750-m radius circle centered on each MODIS pixel, Landsat reference FSC maps (referred to as LandsatFSC) were generated at a 500 m resolution (Dobreva and Klein, 2011; Xiao et al., 2022b). For consistency, FSC values were rescaled to a range of [0, 1].

2.4. IMS snow cover extent products

In this study, we utilized IMS snow cover extent products as a reference to evaluate the effectiveness of our fused FSC estimations in mapping daily snow cover. The IMS, developed by combining multi-source remote sensing data (visible, infrared, and microwave spectra) with other ancillary information, provides binary daily full-spatial coverage snow cover extent maps for the Northern Hemisphere (Helfrich et al., 2007). Daily IMS data with three resolutions (1, 4, and 24 km) were acquired from the NSIDC website, spanning back to 1997. IMS data has undergone extensive validation and has been extensively used in various studies (Chen et al., 2012; Liu et al., 2018; Qiu et al., 2021), consistently demonstrating high accuracy in snow cover classification (>80 %) for the continental United States. This study employed the 1 km resolution IMS data from September 2015 to May 2016. The availability of all relevant data primarily drove the selection of this specific study period.

3. Methodology

3.1. Data fusion framework

Fig. 2 illustrates the workflow diagram of our proposed data fusion framework. This framework addresses the challenge of generating spatiotemporally continuous and fine-resolution FSC data (daily, 1 km) across a continent. It achieves this by employing a multiple-step approach. Given the impossibility of acquiring spatially complete and continuously valid satellite observations over large continental areas, the initial preprocessing is to address missing data in the original FSC grid cells by implementing a spatiotemporal gap-filling method.

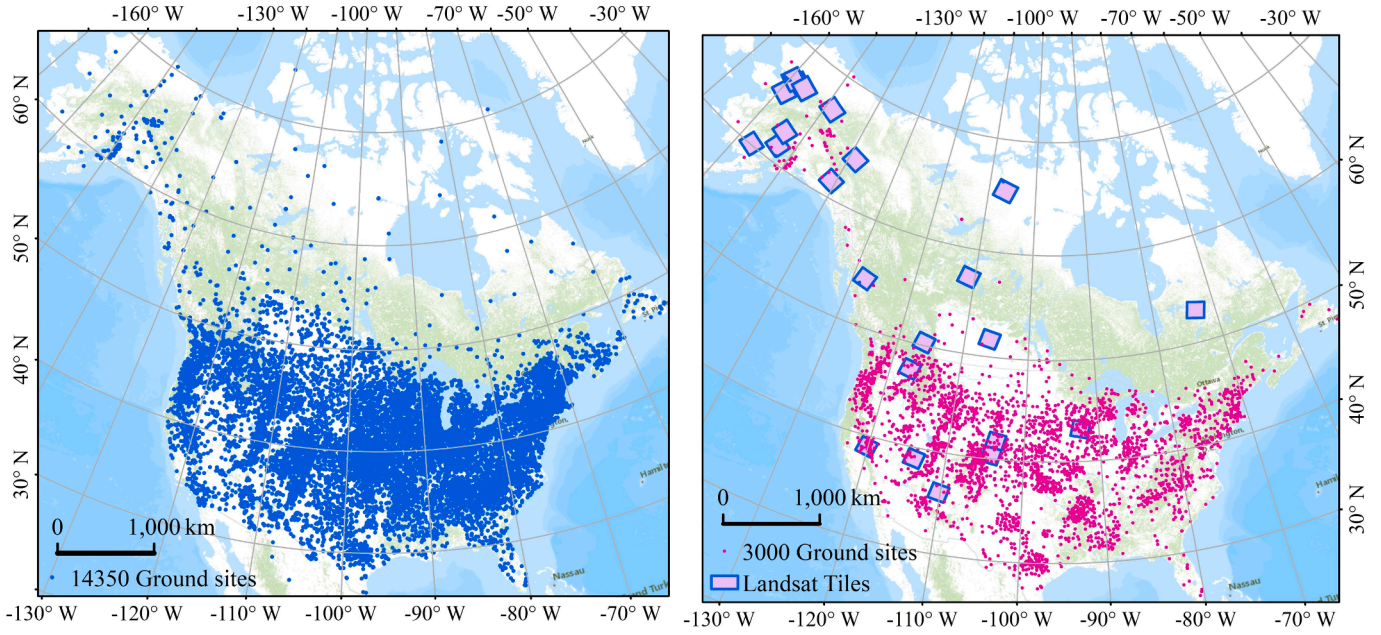

Fig. 1. A map showing the selected snow depth measurements sites (left: 14,350 sites for assessing snow cover mapping capability; right: 3,000 sites for analyzing daily dynamic characteristics of snow cover) over North America and Landsat validation scenes (right).

Subsequently, a novel composited data fusion method is applied for each 1-km grid cell, incorporating information from both satellite FSC data sources. Following with that, a post-processing method as additional refinement step is applied to finally generate a spatiotemporally complete FSC estimation map across the North America region. The effectiveness of this framework in estimating snow cover area is evaluated utilized both fine- (MODIS_FSC, 500 m) and coarse-resolution FSC satellite-based data (PM_FSC, 6.25 km).

Initial preprocessing involved several steps for both MODIS_FSC and PM_FSC data over the North American region. Firstly, MCD12Q1 data was used to identify and eliminate water body pixels. Then, we cleanse the invalid observation labels within both FSC satellite-based data, including scanning strip, cloud, shadow, and polar night labels. Both MODIS_FSC data and PM_FSC data exhibit significant data gaps. These missing values limit the possibility of directly using these datasets within any data fusion method to achieve spatially complete FSC data. Therefore, the third is to implement the spatiotemporal neighborhood cube method (see Section 3.2) for addressing these missing values in both datasets without sacrificing accuracy. While this gap-filling process effectively recovered missing values in PM_FSC data, a substantial proportion of invalid pixels (>20 %) remained in the gap-filled MODIS_FSC data (see Fig. A, Appendix).

To address potential uncertainties inherent in both FSC data, the fourth pre-processing step was employed. Our analysis, along with previous studies (Rittger et al., 2020b; Wang et al., 2021), revealed substantial uncertainties for optical-based FSC values below 0.15. Therefore, following Painter et al. (2009) that assigned all FSC values below 0.15 as 0, we designed experiments to test the influence of this uncertainties in MODIS_FSC on the fused FSC results (Section 4.1), processing or not FSC values below 0.15. Subsequently, we resampled the processed 500 m MODIS_FSC data to a 1 km spatial resolution (MODIS_FSC_1km) using the aggregation method, which is consistent with common practices in previous FSC studies (Czyzowska-Wisniewski et al., 2015; Dobreva et al., 2011; Kuter et al., 2022; Xiao et al., 2022b). Our analysis employed a 1 km resolution instead of 500 m resolution for two key reasons: mitigating errors of MODIS_FSC data and data compatibility with the resolution of IMS snow cover extent products (binary; 1 km). Additionally, to ensure the implement with MODIS_FSC_1km data for the following pixel-by-pixel data fusion, the 6.25 km PM_FSC data was resampled to 1 km spatial resolution using the nearest neighbor resampling method (Long et al., 2019).

To mitigate potential inconsistencies between the two input images, a straightforward local bias correction, which is a linear scaling method, was employed using valid values from MODIS_FSC_1km to adjust the systematic biases of the PM_FSC data (Eq. (1) (Long et al., 2020). Building on Li and Long (2020) and Yu et al. (2023), who emphasized the importance of reducing systematic bias between data sources for obtaining accurate fusion outcomes, we opted for a 3*3 window of 6.25 km pixels for bias correction. This choice balances data fusion accuracy and data processing efficiency, encompassing an area approximately equivalent to 19*19 individual 1 km pixels. Equation (1) details the bias correction method applied to the pixels ($FSC(x,y)_{PM}$) of the coarse-resolution image. This method utilizes the mean values (μ) of its all corresponding neighboring pixels from both the coarse- ($FSC(x_i,y_i)_{PM}$) and fine-resolution ($FSC(x_i,y_i)_{MODIS}$) images within the processing window to obtain corrected the FSC value ($FSC(x,y)'_{PM}$), resulting in PM_FSC_1km. At the date of t, $FSC(x_i,y_i,t)$ represents the FSC values of neighboring pixels in both the coarse-resolution (PM_FSC, denoted by *PM* subscript) and fine-resolution (MODIS_FSC, denoted by *MODIS* subscript) data within the processing window (a 19*19 grids of 1 km pixels centered on $FSC(x,y,t)$).

$$FSC(x,y,t)'_{PM} = FSC(x,y,t)_{PM} + \mu\left(FSC(x_i,y_i,t)_{MODIS}\right) - \mu\left(FSC(x_i,y_i,t)_{PM}\right) \quad (1)$$

In the data fusion stage, an advanced data fusion method (i.e., ESTARFM) was implemented to integrate spatiotemporal information from both FSC datasets. However, its application in large-scale snow cover studies faces two key limitations. Firstly, achieving complete cloud-free input FSC data derived from optical satellite images across whole North America region is practically impossible. Secondly, the inherently dynamic and ephemeral nature of snowpack makes estimating today's snow properties using images captured from months before or after unreliable, as pointed out by Gafurov and Bárdossy (2009). To address these limitations, we first implemented the proposed gap filling method (Section 3.2) to mitigate missing data in two input FSC data caused by various factors (as described above). Secondly, we employed a novel composited ESTARFM method. This method leverages

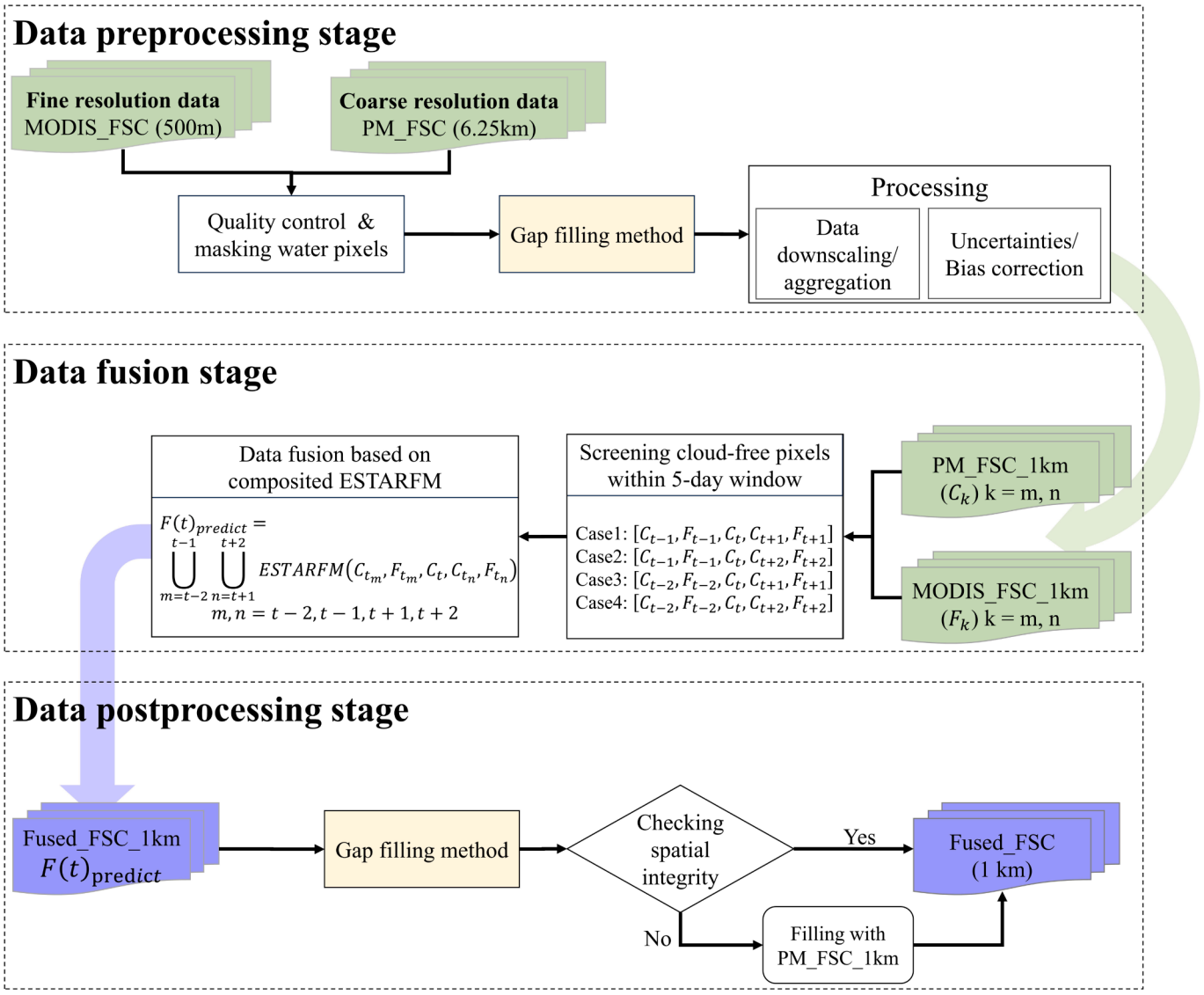

Fig. 2. Workflow diagram for generating spatiotemporally complete fractional snow cover (FSC) data at a 1 km spatial resolution.

the strengths of ESTARFM by combining results from four separate runs. Each run considers images within a 5-day window centered on the predicted date t_p (t_p-2, t_p-1, t_p, t_p+1, t_p+2) (see the discussion in section 5.3). Several studies have shown the effectiveness of leveraging snow cover information from adjacent time steps (short-term) to recover missing data (Gafurov and Bárdossy, 2009; Gao et al., 2010; Xiao et al, 2018). We initially employed image pairs of fine-resolution (F) and coarse-resolution (C) from the nearest neighboring days ($t_p \pm 1$) with ESTARFM to predict the fused FSC value. If a valid value cannot be obtained in the previous step, we iteratively employed ESTARFM method using three additional image pairs combinations: ($C_{t_p-1}, F_{t_p-1}, C_{t_p}, C_{t_p+2}, F_{t_p+2}$), ($C_{t_p-2}, F_{t_p-2}, C_{t_p}, C_{t_p+1}, F_{t_p+1}$), and ($C_{t_p-2}, F_{t_p-2}, C_{t_p}, C_{t_p+2}, F_{t_p+2}$). Processing these combinations are further depicted in Fig. 2 and Eq. (2). By capitalizing ESTARFM's inherent data fusion capabilities and incorporating information from a wider temporal window, our composited method improves the accuracy and the reliability of the final fused FSC results and fortifies the integrity of the fused product. In section 4.4, we incorporated an analysis to offer a more granular understanding of how our data fusion method progressively reduces data gaps.

$$F(t_p) = \bigcup_{m=t_p-2}^{t_p-1} \bigcup_{n=t_p+1}^{t_p+2} ESTARFM(C_{t_m}, F_{t_m}, C_{t_p}, C_{t_n}, F_{t_n}), m, n = t_p-2, t_p-1, t_p+1, t_p+2 \quad (2)$$

Transitioning to the post-processing stage, a series of post-processing procedures was implemented on the fused FSC data derived from data fusion to augment data completeness further. During this stage, we applied the proposed spatiotemporal neighborhood cube method again, but with both a $5 \times 5 \times 3$ cube and a $5 \times 5 \times 5$ cube, to further reduce the proportion of data gaps in the Fused_FSC_1km data. However, in some particular instances, the temporally expanded $5 \times 5 \times 5$ cube may not contain any valid pixels, rendering the spatiotemporal neighborhood cube method ineffective. To address these rare cases, the PM_FSC_1km data was used to fill the remaining data gaps, ultimately achieving a spatiotemporal continuity FSC dataset. This data fusion framework enables the generation of gapless, daily FSC data at 1 km resolution across North American. The entire data processing pipeline was executed on a 2.40 GHz Intel Xeon server.

3.2. Spatiotemporal neighborhood cube for gap filling

A spatiotemporal information cube method was developed to mitigate the presence of data gaps in the FSC data referring to the work of Huang et al. (2018) on binary snow cover. This gap filling method integrates snow cover area information from neighboring pixels across both space and time dimensions. The weighted sum of the values and distances of all pixels within the spatiotemporal neighborhood cube determined the central invalid pixel's value. Fig. 3a illustrates an example of a 3 × 3 × 3 spatiotemporal neighborhood cube at time *t*, comprising a given central pixel and 26 neighborhood pixels in a 3 × 3 spatial domain and a 3-day temporal domain (before the day (*t* − *1*), current day (*t*), after day (*t* + *1*)). The calculation of the given central pixel's value within a 3 × 3 × 3 spatiotemporal neighborhood cube is expressed as Eq. (3). In cases no valid pixels (0 ≤ FSC≤1) are available when executing a 3 × 3 × 3 spatiotemporal neighborhood cube, the cube is first expanded spatially to a 5 × 5 × 3 spatiotemporal neighborhood cube to ensure adequate valid data coverage (Fig. 3b). If the 5 × 5 × 3 spatiotemporal neighborhood cube still lacks valid pixels, the cube is further extended temporally to a 5 × 5 × 5 spatiotemporal neighborhood cube to enhance valid data availability (Fig. 3c). Otherwise, the given central pixel is assigned an invalid value.

$$FSC_{center} = \begin{cases} \sum_{-1}^{1}\sum_{-1}^{1}\sum_{-1}^{1} \frac{Dis(x,y,t) \times FSC(x,y,t)}{\sum_{i=1}^{n} Dis(x,y,t)}, for 3 \times 3 \times 3 cube \\ \sum_{-2}^{2}\sum_{-2}^{2}\sum_{-1}^{1} \frac{Dis(x,y,t) \times FSC(x,y,t)}{\sum_{i=1}^{n} Dis(x,y,t)}, for 5 \times 5 \times 3 cube \\ \sum_{-2}^{2}\sum_{-2}^{2}\sum_{-2}^{2} \frac{Dis(x,y,t) \times FSC(x,y,t)}{\sum_{i=1}^{n} Dis(x,y,t)}, for 5 \times 5 \times 5 cube \end{cases} \quad (3)$$

$$Dis(x,y,t) = \sqrt{x^2 + y^2 + kt^2} \quad (4)$$

The position of (x,y,t) in Eq. (3) corresponds to the relative position with respect to the "central pixel" (Fig. 3); (x,y) denotes the spatial location, while t represents the time. These coordinates take discrete values relative to the "central pixel" (±2, ±1, and 0). $FSC(x,y,t)$ denoted the FSC value at the specific position (x,y,t). The spatiotemporal weight assigned to each valid pixel is inversely proportional to its distance from the central pixel. $Dis(x,y,t)$ represents the 3D Euclidean distance between the "central pixel" and its neighborhood pixels. In Eq. (4), k denotes the weight assigned to the temporal distance relative to the spatial distance and was set to 3 according to Huang et al. (2018).

3.3. ESTARFM

The Spatial and Temporal Adaptive Reflectance Fusion Model (STARFM) (Gao et al., 2006) is a well-established data fusion method applicable to homogeneous and heterogeneous conditions. To further enhance its predictive power in heterogeneous landscapes, Zhu et al. (2010) developed the ESTARFM, a widely employed technique for integrating diverse data sources to generate fine-resolution, highly accurate estimations. Five available images is necessary for the ESTARFM method, consisting of a coarse-resolution FSC image (C_{t_p}) at time t_p, as well as two pairs of FSC image consisting of fine-resolution (F_{t_m}) and corresponding coarse-resolution (C_{t_m}) images, and fine-resolution (F_{t_n}) and corresponding coarse-resolution (C_{t_n}) images, captured at time t_m and time t_n, respectively. ESTARFM assumes a linear relationship between the fine- and coarse-resolution image pairs at any given time. The fine-resolution images serve as a baseline for determining the absolute FSC value at time t_p, whereas coarse-resolution images provide temporal variation information of FSC. By employing a linear spectral mixing model (Eq. (5), the fused FSC value at time t_p can be predicted by using two pairs of fine-resolution FSC data and coarse-resolution FSC data at time t_m and time t_n. The calculation of the fine-resolution FSC value at the central pixel ($F\left(x_{w/2}, y_{w/2}, t_p\right)$) incorporates FSC information from all similar pixels within the search window by considering both their spatial weight ($W_i v_i$) and temporal weight (T_k), as detailed in Eq. (6). Fig. B provides a visual representation of this entire calculation process for the central pixel's FSC value. To simplify the ESTARFM method, Eq.

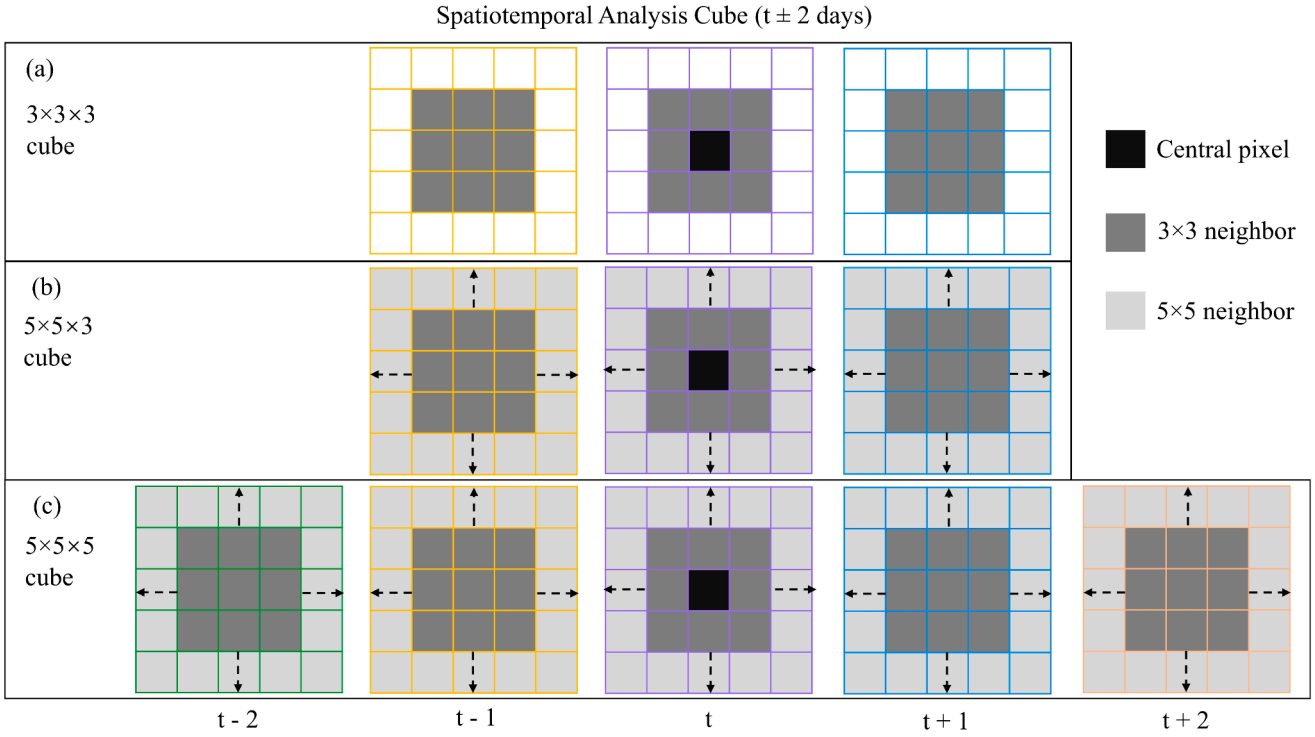

Fig. 3. The spatiotemporal cubic neighborhood schematic. *t* denotes time; (a) default 3 × 3 × 3 spatiotemporal cube; (b) spatially extended 5 × 5 × 3 spatiotemporal cube; (c) spatially and temporally extend 5 × 5 × 5 spatiotemporal cube.

(5) and Eq. (6) can be condensed into Eq. (7), which takes as inputting five images captured at times t_m, t_p, and t_n (i.e., $C_{t_m}, F_{t_m}, C_{t_p}, C_{t_n}, and F_{t_n}$).

$$F\left(x_{w/2}, y_{w/2}, t_p\right) = T_m \times F_m\left(x_{w/2}, y_{w/2}, t_p\right) + T_n \times F_n\left(x_{w/2}, y_{w/2}, t_p\right) \quad (5)$$

$$F_k\left(x_{w/2}, y_{w/2}, t_p\right) = F\left(x_{w/2}, y_{w/2}, t_k\right) + \sum_{i=1}^{N} W_i v_i \times \left(C\left(x_i, y_i, t_p\right) - C\left(x_i, y_i, t_k\right)\right), (k = m, n) \quad (6)$$

$$F\left(t_p\right) = ESTARFM\left(C_{t_m}, F_{t_m}, C_{t_p}, C_{t_n}, F_{t_n}\right) \quad (7)$$

where F and C represent the FSC data at fine- and coarse- resolutions, respectively. The central pixel within the search window is denoted as $\left(x_{w/2}, y_{w/2}\right)$, where w indicates the window size. N represents the number of similar pixels, and (x_i, y_i) represents their respective location. The similar pixels were identified within the searching window (See Eq. (8) based on the standard deviation of FSC values (σ) and the land cover classes (b), which was set as 4 classes based on our previous study (Xiao et al., 2021). The conversion factor v_i of similar pixel i is derived by regressing the fine-resolution FSC value against the corresponding coarse-resolution FSC values of the similar pixels falling within the same coarse-resolution pixel. Weight W_i describes the contribution of similar pixel i to the central pixel's FSC value $\left(x_{w/2}, y_{w/2}\right)$. It is determined by considering the relative location of the similar pixel i to the central pixel and the snow cover distribution similarity between fine-resolution FSC (F_k) and coarse-resolution FSC (C_k) values (Eqs. (9)–(12). The temporal weights T_k (Eq. (13) are calculated by measuring the magnitude of changes in the coarse-resolution FSC (C_k) between time t_k ($k = m, n$) and the prediction time t_p. For more detailed this calculation procedure explanation and method description, please refer to Zhu et al. (2010).

$$\left|F(x_i, y_i, t_k) - F\left(x_{w/2}, y_{w/2}, t_k\right)\right| \le 2\sigma/b \quad (8)$$

$$W_i = (1/D_i)/\sum_{i=1}^{N}(1/D_i) \quad (9)$$

$$D_i = (1 - R_i) \times d_i \quad (10)$$

$$R_i = \frac{E[(F_i - E(F_i))(C_i - E(C_i))]}{\sqrt{Var(F_i)} \times \sqrt{Var(C_i)}} \quad (11)$$

$$d_i = 1 + \sqrt{\left(x_{w/2} - x_i\right)^2 + \left(y_{w/2} - y_i\right)^2}/(w/2) \quad (12)$$

$$T_k = \frac{1/\left|\sum_{j=1}^{w}\sum_{l=1}^{w} C(x_j, y_l, t_k) - \sum_{j=1}^{w}\sum_{l=1}^{w} C(x_j, y_l, t_p)\right|}{\sum_{k=m,n}\left(1/\left|\sum_{j=1}^{w}\sum_{l=1}^{w} C(x_j, y_l, t_k) - \sum_{j=1}^{w}\sum_{l=1}^{w} C(x_j, y_l, t_p)\right|\right)} \quad (13)$$

The ESTARFM method was originally designed for surface reflectance data fusion of satellite imagery with different resolutions. However, its principles, such as the assumed linear relationship between fine and coarse resolution data, similarity pixel identification thresholds, and calculation of spatial and temporal weights, hold applicability for broader data fusion tasks. Notably, the ESTARFM has demonstrated success in data fusion tasks involving variable with gradual temporal changes, such as surface temperature, water vapor, soil moisture, vegetation index (Normalized Difference Vegetation Index, NDVI), and snow index (NDSI) (Bousbaa et al., 2022; Kong et al., 2021; Li and Long, 2020; Long et al., 2020, 2019; Nietupski et al., 2021; Yu et al., 2023; Zhu et al., 2010). These variables exhibit smooth and continuous variations over time, aligning with the core assumption of the ESTARFM method.

However, FSC variable exhibits inherent variability due to abrupt changes caused by snowfall events or rapid snowmelt. This characteristic raises concerns about the suitability of the ESTARFM method for generating high-resolution and spatiotemporally complete FSC data. The capability of ESTARFM to handle this variability of FSC remains under investigation. Several limitations hinder the applications of ESTARFM method for sub-pixel snow cover area estimation, especially across vast regions. Firstly, systematic biases between data sources can be potentially introduced by differences in retrieval algorithms, observation sources (e.g., sensor types), and observation geometry. ESTARFM's prediction accuracy heavily relies on the quality and comparability of the coarse- and fine-resolution datasets. Secondly, spatial gaps in input data (either coarse- or fine-resolution data) can lead to missing values in the fused product. This has limited previous applications to smaller or mid-latitude regions with better data availability. Finally, unique snow characteristics present distinct interpretations for zero values (snow-free) and non-zeros values (snow-covered), unlike the prior predictor variables typically used with ESTARFM. Additionally, the dynamic and ephemeral nature of snow cover makes using data from months before or after highly unreliable for estimating current snow properties. Consequently, addressing these challenges become crucial for successfully applying the ESTARFM method to map snow cover area across large regions.

Hence, our primary objective is to adapt the ESTARFM algorithm to better capture spatiotemporal dynamics of snow cover and to generate high-resolution, daily FSC mapping across vast areas. To overcome these limitations and enhance fusion accuracy, we implemented the following strategies: 1) We employ Eq. (1) to adjust systematic biases within coarse-resolution input data using corresponding fine-resolution input data within each processing window. This ensures uncertainty consistency of input data and minimizes errors in the final fused FSC values (refer to Eq. (1). 2) To address data gaps, a spatiotemporal neighborhood gap-filling method (detailed in Section 3.2) is used to reconstruct missing information in both coarse- and fine-resolution input images. Moreover, a novel composite ESTARFM method (illustrated by Eq. (2) strengthens the integrity of the fused FSC product. 3) To minimize errors arising from input data selection and account for rapid snow cover changes, we incorporate snow cover information from adjacent days (±2 days) into data fusion process (see Eq. (2), rather than relying on data from distant timepoints. This study presents a groundbreaking data fusion framework by pioneering the use of a modified ESTARFM algorithm for both spatial and temporal fusion of FSC data. Our framework tackles the specific challenges associated with applying ESTARFM to snow cover mapping, enabling the generation of spatially and temporally complete FSC data for North America. Section 5.3 delves deeper into the application of ESTARFM algorithm in snow cover study.

3.4. Evaluation of fractional snow cover results

3.4.1. Statistical metrics for evaluating the fractional and binary values

To evaluate the fused FSC estimations, we utilized Landsat reference FSC and employed the correlation coefficient (R), mean absolute error (MAE), and root-mean-square-error (RMSE) as statistical metrics (Xiao et al., 2021). These three metrics were also used to evaluate the ability of snow cover products to capture snow cover evolution when using snow cover-phenology metrics (see Section 3.6.2) throughout the entire snow cover season.

In another evaluation, to establish a direct comparison between the FSC and the snow depth observations, both snow depth values and FSC values were converted into binary values, where the snow depth threshold of 2 cm and the FSC threshold of 0.3 were used to binarize a value as either snow-covered (1) or snow-free (0) (Xiao et al., 2021), respectively. Specifically, the description can be formulized by SC=1 if FSC≥0.3 or snow depth ≥ 2 cm. The binarized snow cover results were evaluated using six accuracy metrics (Xiao et al., 2021): overall accuracy (OA), precision, recall, specificity, F1_score, and Cohen's kappa coefficient (Cristea et al., 2017). The optimal values for OA, F1_score, and Kappa were 1, with 0 representing the worst performance.

3.4.2. Snow-cover phenology metrics for characterizing daily snow dynamics

The evaluation and validation conducted in Section 3.4.1 focused on the overall performance without considering the daily dynamic characteristics of snowpacks. However, this study produces the daily FSC data with spatially complete snow cover distribution information. There is a lack of fine-resolution continuous snow observations apart from ground-based snow depth measurements. To comprehensively assess the daily dynamic performance of daily snow cover data, i.e., the fused FSC data and IMS snow cover extent product, this section employs a novel evaluation method using snow-cover phenology metrics (Fig. 4). Ground-based snow depth daily observations from 3000 sites served as a reference benchmark for these metrics.

Fig. 4 provides a visual depiction of the snow-cover phenology metrics definition employed in this study, which includes snow cover duration, snow onset date, snow end date, and snow cover days (Chen et al., 2015; Klein et al., 2016). In this context, a snow cover year was defined as the period from September of a given year to June of the following (Fig. 4). The snow onset date was identified as the first day of the first five consecutive days period with snow cover. Conversely, the snow end date was determined as the first day after the last five consecutive days period without snow cover. Furthermore, the snow cover duration represents the number of days between the onset and end dates of snow cover. The total number of snow days from the snow onset date to the snow end date was defined as snow cover days.

4. Results

4.1. Accuracy evaluation of the fused fractional snow cover

The selected Landsat-FSC derived data (referred to as LandsatFSC) under clear-sky conditions were employed to assess the performance of the fused FSC (FusedFSC) and the fine-resolution input data (i.e., MODIS_FSC_1km) at a 1 km spatial resolution. It should be noted that the MODIS_FSC_1km data is derived from the original MODIS_FSC (500 m) data through a multi-step process. Evaluation results using nine of 24 Landsat scenes are presented in this section (Table 2 and Figs. 5 and 6), while the remaining evaluation results for 15 scenes are provided in the Appendix (Table B and Fig. C).

As input data of the data fusion model, MODIS_FSC_1km data demonstrate strong performance in FSC estimation, exhibiting high correlation with LandsatFSC (R=0.64–0.92) and low errors (MAE=8.7–16.7 %, RMSE=9.9–18.9 %), as depicted in Fig. 6. The overall performance of MODIS_FSC_1km is characterized by low errors (MAE=12.6 %, RMSE=15.1 %; Table 2). These evaluation results confirm that the input data (MODIS_FSC_1km) exhibit reliable overall accuracy with low errors with reference to LandsatFSC. By employing two input FSC datasets, the daily continuous FusedFSC was generated through the proposed data fusion framework. Evaluation results of FusedFSC data on nine Landsat scenes (Table 2 and Fig. 5) reveal a comparable accuracy to MODIS_FSC_1km, with high correlation (R=0.62–0.94) and low errors (MAE=8.5–15.0 %, RMSE=9.8–17.0 %). Further assessment of 15 Landsat scenes further underscores the superior performance of FusedFSC data in estimating FSC, with low bias (RMSE=6.8–18.9 %; Table B1 in the Appendix). Cases of comparisons between MODIS_FSC_1km and FusedFSC on nine scenes (Table 2 and Figs. 5–6) illustrate the slightly improved accuracy of FusedFSC in capturing spatial variation in FSC compared to MODIS_FSC_1km. Evaluation conducted on 24 Landsat scenes demonstrates the effectiveness of the proposed data fusion framework in generating daily continuous FSC estimates with high accuracy under clear-sky conditions.

Our analysis compares FusedFSC and MODIS_FSC_1km data and finds that they exhibited comparable performance in FSC estimation. However, studies by Rittger et al. (2020b) and Wang et al. (2021) suggest that estimation errors tend to be higher for low FSC values, particularly those below 0.15. Therefore, we investigated the impact of

Table 2
Summary of accuracy metrics for the fused fractional snow cover data (FusedFSC) and the fine-resolution input data (MODIS_FSC_1km) using the nine Landsat scenes FSC data as the reference data. (a)-(i) denote the ID of Landsat scenes (cf. Table A in the Appendix).

ID of Landsat scene	Data name	R	MAE	RMSE
All nine scenes	FusedFSC	0.91	11.6 %	14.1 %
	MODIS_FSC_1km	0.91	12.6 %	15.1 %
(a)	FusedFSC	0.73	15.0 %	17.3 %
	MODIS_FSC_1km	0.71	16.7 %	18.9 %
(b)	FusedFSC	0.94	9.8 %	13.2 %
	MODIS_FSC_1km	0.92	11.9 %	15.3 %
(c)	FusedFSC	0.93	13.3 %	17.0 %
	MODIS_FSC_1km	0.92	14.8 %	18.3 %
(d)	FusedFSC	0.91	12.4 %	13.9 %
	MODIS_FSC_1km	0.90	13.5 %	15.0 %
(e)	FusedFSC	0.91	13.7 %	15.9 %
	MODIS_FSC_1km	0.91	13.5 %	15.8 %
(f)	FusedFSC	0.87	13.5 %	15.9 %
	MODIS_FSC_1km	0.85	14.8 %	16.9 %
(g)	FusedFSC	0.71	8.5 %	9.8 %
	MODIS_FSC_1km	0.71	8.7 %	9.9 %
(h)	FusedFSC	0.62	9.5 %	11.0 %
	MODIS_FSC_1km	0.64	9.7 %	11.0 %
(i)	FusedFSC	0.88	9.7 %	11.8 %
	MODIS_FSC_1km	0.86	10.9 %	13.0 %

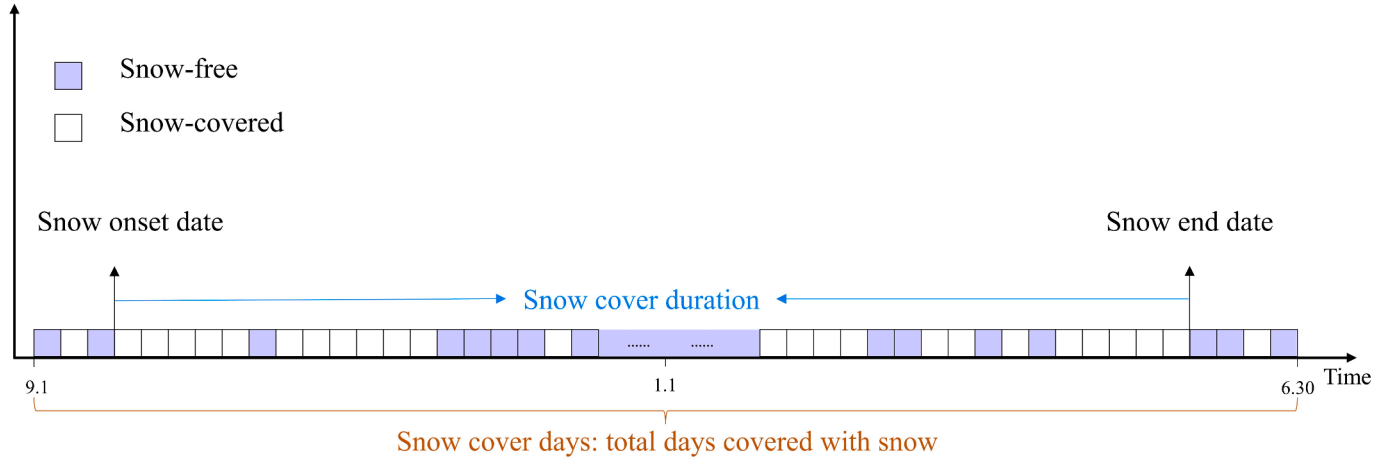

Fig. 4. Diagram of snow-cover phenology metrics, spanning from September of a given year to June of the following year, including snow cover duration, snow onset date, snow end date, and snow cover days.

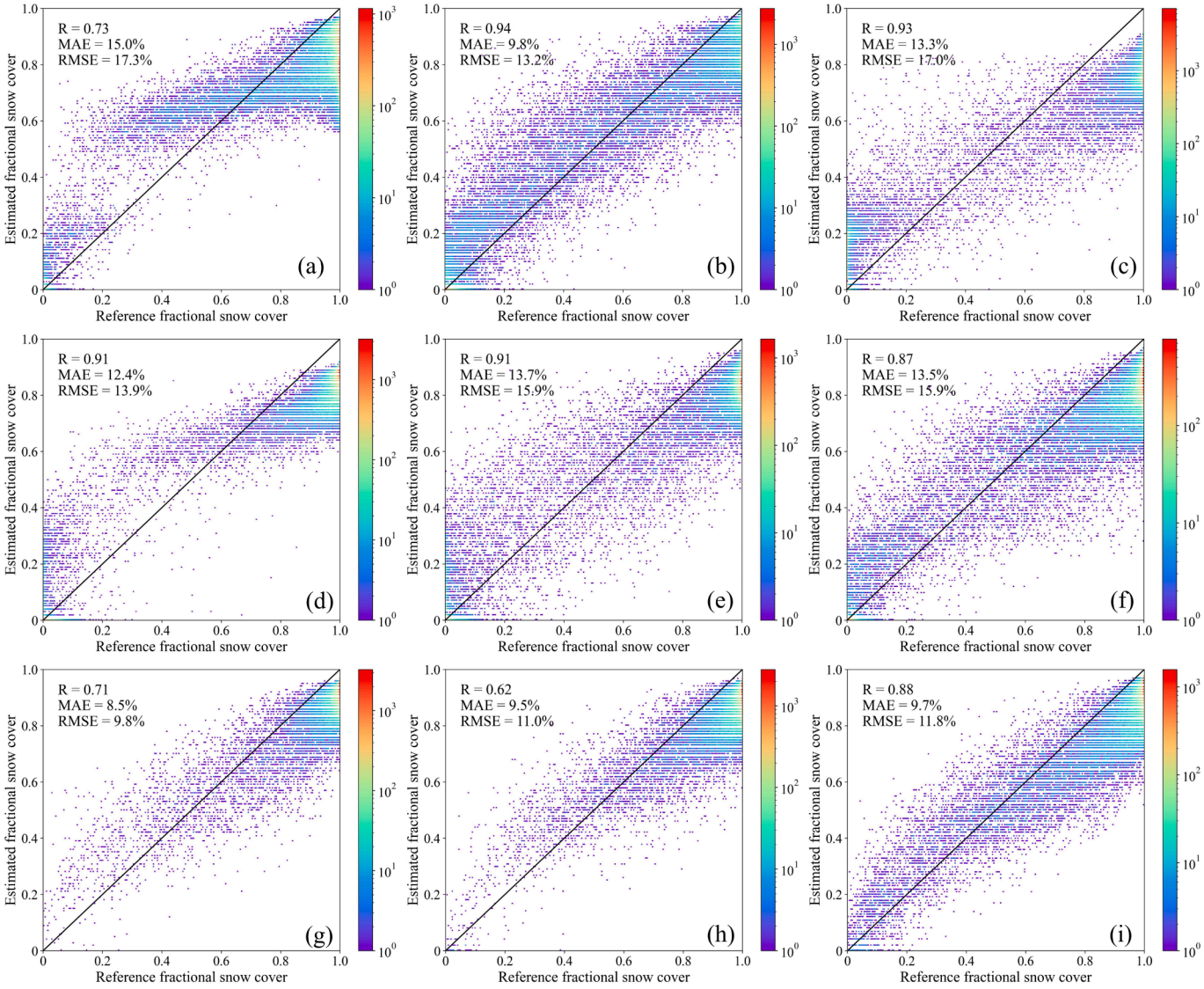

Fig. 5. Scatter plot of Landsat reference fractional snow cover (x-axis) versus the fused fractional snow cover (FusedFSC, y-axis) for the nine scenes (cf. Fig. C in the Appendix and Table 3), with a 1:1 line shown. (a)-(i) denote the ID of Landsat scenes (cf. Table A in the Appendix). FSC is a unitless variable.

processing or not FSC values below 0.15 assigned as 0 on FusedFSC data. Three Landsat scenes with varying degrees of snow cover fraction (low, moderate, and high) were selected for the analysis (Fig. 7). Table 3 and Fig. 8 present the results of comparing FusedFSC data and LandsatFSC data.

The first to third rows of Fig. 7 display the snow cover distribution as measured by LandsatFSC, MODIS_FSC, and FusedFSC, respectively. The last row describes the error of FusedFSC compared to LandsatFSC, where green and purple represent positive and negative biases, respectively. Our analysis revealed that overestimation pixels are predominantly located in areas with lower FSC (blue), while underestimation pixels are consistent with the presence of higher FSC (red). When FSC values below 0.15 in MODIS_FSC data were processed by assigning them to 0, FusedFSC data exhibits lower errors (Table 3; RMSE: 16.0 % vs. 15.3 %, 15.4 % vs. 15.0 %). Moreover, the spatial distribution of snow cover in FusedFSC more closely resembled that of LandsatFSC data. Fig. 8 further illustrates the difference between processing and not processing FSC values below 0.15 for MODIS_FSC and FusedFSC. The impact of processing low FSC values was pronounced in the Landsat scene with a higher proportion of patch snow (Scene ID: 03303220160122; Table 3; first column of Fig. 8). In contrast, the Landsat scene with relatively few low FSC values (Scene ID: 07701320160415) showed minimal changes in the fused result when processing or not processing these values (third column of Fig. 8; RMSE: 9.9 % vs. 9.9 %; MAE: 8.7 % vs. 8.7 %). These findings suggest that processing FSC values below 0.15 contributes to improved consistency and robustness of the FusedFSC estimation. By removing these potential erroneous values, the data fusion framework is better able to capture the true spatial distribution of snow cover and provide more accurate estimates of FSC.

4.2. *Validation analysis based on ground-based observations*

4.2.1. *Snow cover mapping capability*

While the evaluation and analysis of FusedFSC data primarily rely on clear-sky Landsat imagery, ground-based snow depth observations offer valuable insights into surface snow cover distribution under diverse weather conditions. Therefore, we employed a total of 1,835,823 snow depth observational records from 14,350 sites collected between September 2015 and May 2016 to assess the performance of FusedFSC data and IMS snow cover extent products. Table 4 and Fig. 9 present the binarized snow validation results in terms of accuracy metrics for 14 land cover types classified according to the MOD12Q1 Annual International Geosphere-Biosphere Programme (IGBP) classification scheme. Due to the limited availability of ground observation records, accuracy

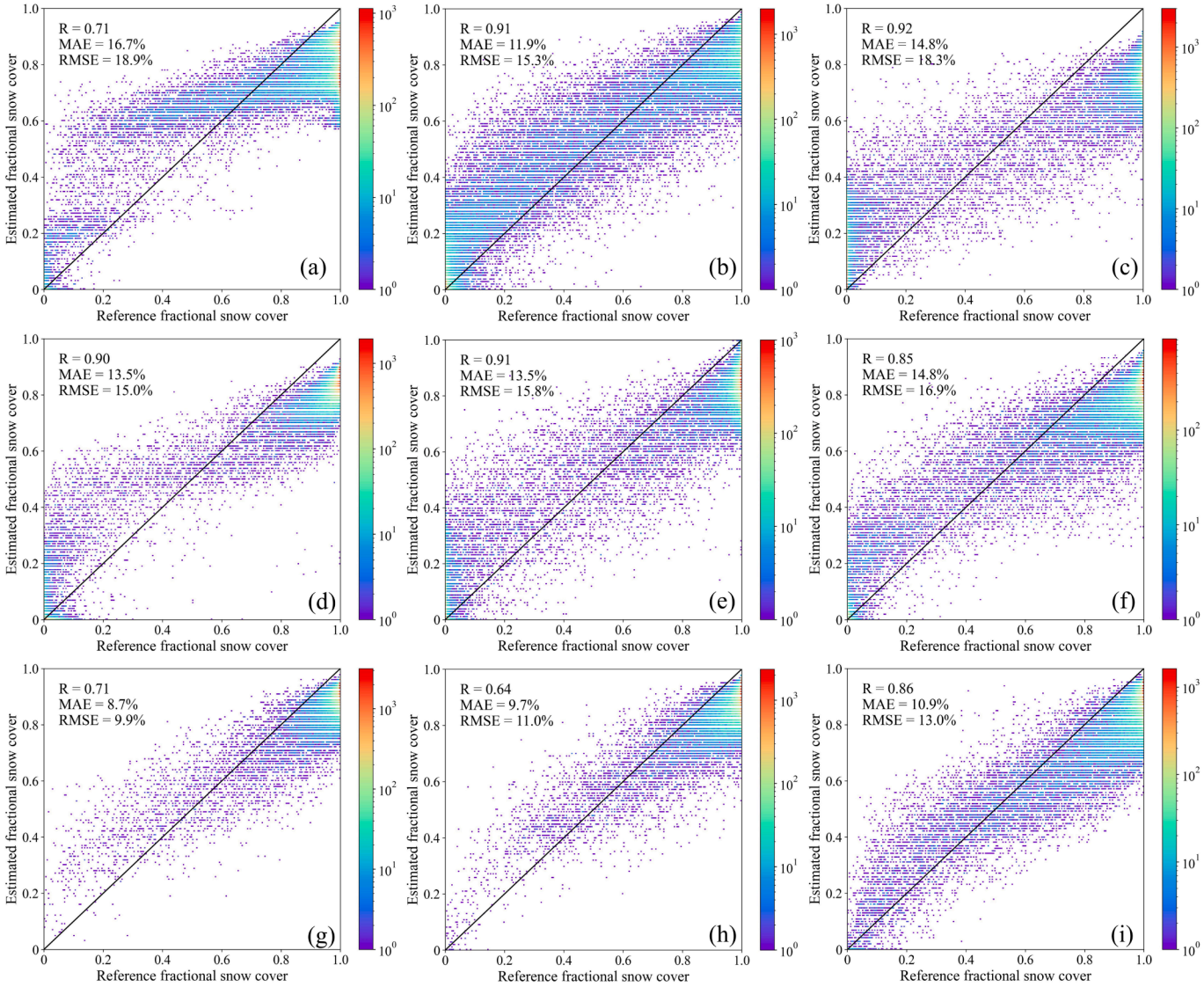

Fig. 6. Scatter plot of Landsat reference fractional snow cover (x-axis) versus the MODIS_FSC_1km fractional snow cover (y-axis) for the nine scenes (cf. Fig. C in the Appendix and Table 3), with a 1:1 line shown as well. (a)-(i) denote the ID of Landsat scenes (cf. Table A in the Appendix). FSC is a unitless variable.

metrics for the broadleaf evergreen forest and permanent snow ice classes are not included.

The OA and Kappa coefficient values for the binarized FusedFSC range from 0.84 to 0.98 and 0.68 to 0.88, respectively, while those for IMS data span from 0.86 to 0.96 and 0.70 to 0.82. As evident from Table 4 and Fig. 9, the binarized FusedFSC demonstrates slightly superior accuracy, with an OA of 0.92 compared to 0.91 for IMS. This enhanced accuracy was corroborated by a higher Kappa coefficient of 0.80 for FusedFSC, compared to 0.70 for IMS. Moreover, the binarized FusedFSC data exhibit lower commission errors (CE) and omission errors (OE), with values of 0.19 and 0.10, respectively, compared to 0.21 and 0.12 for IMS products. In terms of snow cover mapping during the period from 2015 to 2016, IMS data surpassed FusedFSC only for evergreen needleleaf forest types, with higher OA (0.86 for IMS vs. 0.84 for FusedFSC) and Kappa (0.71 for IMS vs. 0.68 for FusedFSC). Overall, the binarized FusedFSC consistently outperformed IMS snow cover products for most land cover types in accurately identifying snow cover.

4.2.2. Daily dynamic characteristic of snow cover using snow-cover phenology metrics

The FusedFSC and IMS data provide comprehensive and continuous daily snow cover information. While the preceding section examined the spatial accuracy of these datasets, this section employed ground-based snow depth measurements from 3,000 continuous daily observation sites to assess the reliability of these two products in characterizing the temporal dynamics of snow cover over a daily time series. Four snow-cover phenology metrics (Fig. 4) were calculated within a snow cover year for the ground-based measurements from 3,000 sites, FusedFSC data, and IMS products. Figs. 10 and 11 depict the error distributions and associated summary accuracies for these four snow-cover phenology metrics, comparing FusedFSC and IMS data against a reference benchmark established using ground-based phenology metrics. The analysis revealed that the error distributions of the binarized FusedFSC data were relatively concentrated near zero (Fig. 10), indicating high precision. Additionally, FusedFSC data consistently demonstrated lower errors (RMSE and MAE) and higher correlation (R) for four phenology metrics compared to IMS data (Fig. 11). Among the four metrics (Fig. 10), the error density of snow onset date was found to be highest around zero, suggesting both daily snow cover products were highly accurate in describing the onset of snow cover. This observation is further supported by the RMSE values for snow onset date, snow end date, snow cover duration, and snow cover days (Fig. 11). For FusedFSC, the RMSE values are 16.2, 17.3, 24.9, and 18.8 days, respectively, compared to 16.7, 21.2, 29.8, and 25.2 days for IMS data. Based on this comprehensive

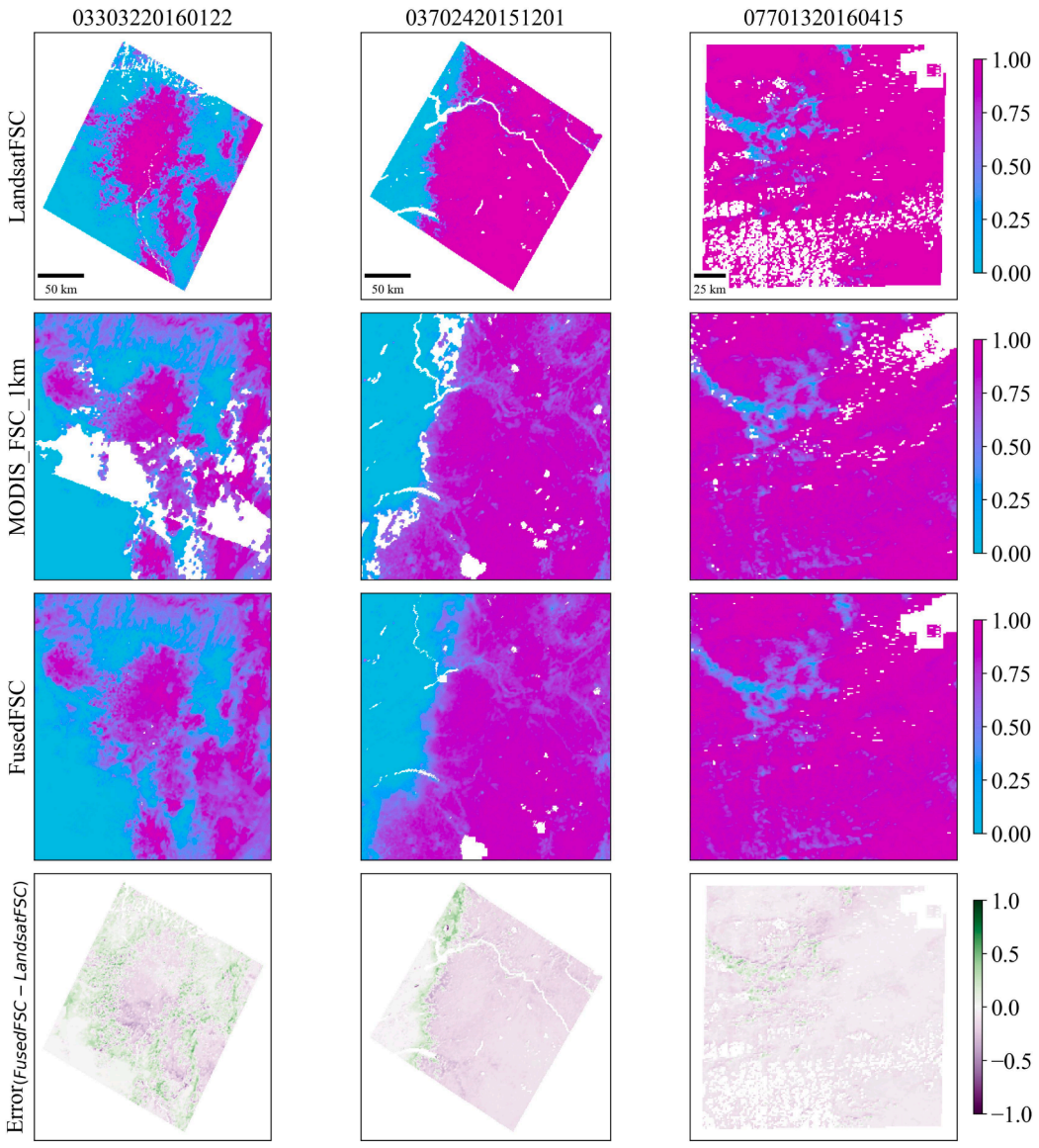

Fig. 7. The influence analysis of MODIS_FSC_1km accuracy on the fused fractional snow cover (referred to as FusedFSC) compared to three LandsatFSC scenes. In this case, the values of MODIS_FSC below 0.15 were assigned as 0.

Table 3
Summary of accuracy metrics demonstrating the influence of MODIS_FSC accuracy on the fused FSC against the Landsat reference FSC for three scenes. The "Not processing" (NP) column denotes that the FSC values below 0.15 of the fine-resolution input data (MODIS_FSC_1km) were not processed, while the "Processing" (P) column denotes that these values were assigned as 0.

	03,303,220,160,122		03,702,420,151,201		07,701,320,160,415	
	NP	P	NP	P	NP	P
R	0.91	0.92	0.90	0.90	0.71	0.71
MAE	13.5 %	11.9 %	14.3 %	13.5 %	8.7 %	8.7 %
RMSE	16.0 %	15.3 %	15.4 %	15.0 %	9.9 %	9.9 %

assessment, it is evident that the binarized FusedFSC data provide a more accurate and consistent representation of daily snow cover dynamics compared to IMS data, closely aligning with ground-based observations.

4.3. Spatiotemporal distribution of the fused fractional snow cover across North America

We conducted a comparative analysis of the spatial performance between MODIS_FSC_1km and FusedFSC at the fusion unit (1 km) in three Landsat scene regions (Fig. 12) and across North America (Fig. 13). The comparison dates were chosen on the 15th of every month from September 2015 to May 2016. Despite incorporating a gap-filling method (Section 3.2), MODIS_FSC_1km snow cover maps in Figs. 12 and 13 still displayed a considerable number of no-data pixels (>30 % of the entire study area) on most days, hindering spatiotemporal snow cover analysis. Conversely, FusedFSC in Figs. 12 and 13 present complete spatial features and accurately capture the distribution of snow cover. Moreover, FusedFSC convincingly aligns with the spatial pattern of MODIS_FSC_1km within each Landsat scene region under clear-sky conditions, indicating the effectiveness of the proposed data fusion framework in estimating FSC. Fig. 14 further depicts the data integrity percentage of FusedFSC data, illustrating the contributions of the data fusion framework, encompassing various methods, to achieve spatial completeness. The results clearly revealed that the composited

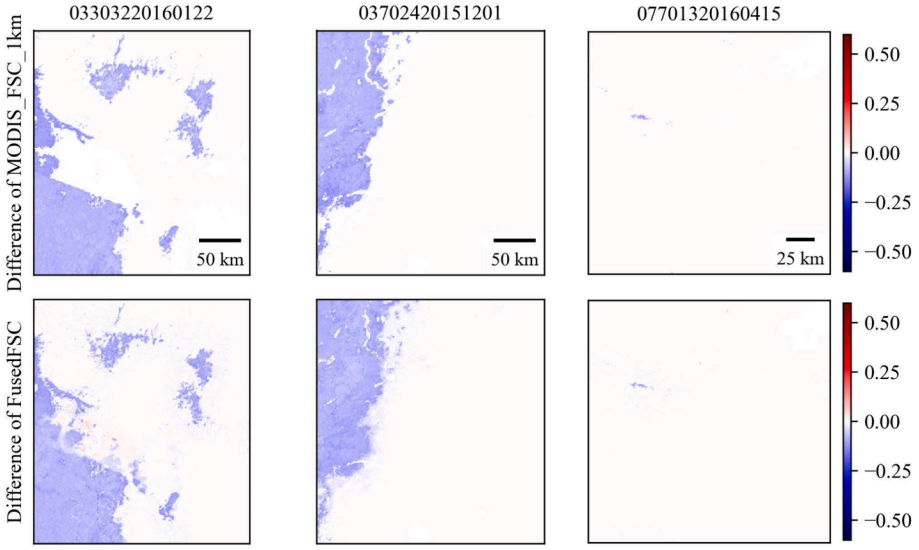

Fig. 8. The difference with and without processing the values of MODIS_FSC_1km below 0.15 for MODIS_FSC_1km and the fused FSC (referred to as FusedFSC) in three Landsat scenes (cf. Fig. 7). Negative values (depicted in blue) indicate that the results of the "Processing" approach are lower than those of the "Not processing" approach, and vice versa. (For interpretation of the references to colour in this figure legend, the reader is referred to the web version of this article.)

Table 4
Validation results for snow cover mapping capability of binarized snow cover derived from fused fractional snow cover (FusedFSC) data and the IMS snow cover extent data. The evaluation of the snow cover mapping capability of FusedFSC and IMS data was conducted across 14 land cover types using a comprehensive dataset of 1,835,823 snow depth measurement records gathered from 14,350 ground observation sites. The number of ground snow depth records available for the evergreen broadleaf forests type is limited and, therefore, not displayed in the table. The abbreviations ENF (evergreen needleleaf forests), NDF (deciduous needleleaf forests), DBF (deciduous broadleaf forests), CS (closed shrublands), OS (open shrublands), PW (permanent wetlands), CNVM (cropland or natural vegetation mosaics), and UBL (urban and built-up lands) are provided for reference.

Land cover types	Data name	OA	Precision	Recall	Specificity	F1_score	Kappa
All samples	FusedFSC	0.92	0.81	0.90	0.93	0.86	0.80
	IMS	0.91	0.79	0.88	0.92	0.83	0.77
ENF	FusedFSC	0.84	0.79	0.84	0.84	0.81	0.68
	IMS	0.86	0.90	0.75	0.94	0.82	0.71
DNF	FusedFSC	0.93	0.90	0.95	0.92	0.93	0.87
	IMS	0.88	0.93	0.78	0.95	0.85	0.75
DBF	FusedFSC	0.92	0.80	0.78	0.96	0.79	0.74
	IMS	0.92	0.75	0.86	0.94	0.80	0.75
Mixed Forests	FusedFSC	0.90	0.79	0.91	0.90	0.85	0.78
	IMS	0.90	0.80	0.89	0.90	0.84	0.77
CS	FusedFSC	0.86	0.72	0.91	0.83	0.81	0.70
	IMS	0.87	0.83	0.77	0.92	0.79	0.70
OS	FusedFSC	0.98	0.86	0.93	0.98	0.89	0.88
	IMS	0.96	0.79	0.84	0.97	0.81	0.79
Woody savannas	FusedFSC	0.93	0.85	0.92	0.93	0.89	0.83
	IMS	0.91	0.84	0.88	0.93	0.86	0.80
Savannas	FusedFSC	0.94	0.87	0.93	0.95	0.90	0.86
	IMS	0.93	0.85	0.90	0.94	0.87	0.82
Grassland	FusedFSC	0.93	0.85	0.91	0.93	0.88	0.83
	IMS	0.90	0.80	0.88	0.91	0.84	0.77
PW	FusedFSC	0.92	0.78	0.95	0.90	0.86	0.80
	IMS	0.90	0.83	0.78	0.94	0.81	0.74
Croplands	FusedFSC	0.93	0.74	0.92	0.93	0.82	0.78
	IMS	0.91	0.69	0.92	0.91	0.79	0.73
UBL	FusedFSC	0.92	0.73	0.88	0.93	0.80	0.75
	IMS	0.91	0.69	0.86	0.92	0.76	0.71
CNVM	FusedFSC	0.93	0.72	0.91	0.93	0.80	0.76
	IMS	0.91	0.67	0.91	0.92	0.77	0.72
Barren	FusedFSC	0.94	0.75	0.96	0.94	0.84	0.81
	IMS	0.93	0.73	0.93	0.93	0.81	0.77

ESTARFM method, using five days of data, significantly contributes to more than two-thirds (68.1 %) of the complete data. The remaining data gaps (31.9 %) require a postprocessing approach for filling. In comparison to the ESTARFM method, the composited ESTARFM method, with two additional days of data, effectively reduces the substantial proportion of missing information by 10 %. Based on our comprehensive evaluation results, FusedFSC unequivocally demonstrates the remarkable performance of the proposed data fusion framework in producing spatially complete and temporally continuous FSC data across North America.

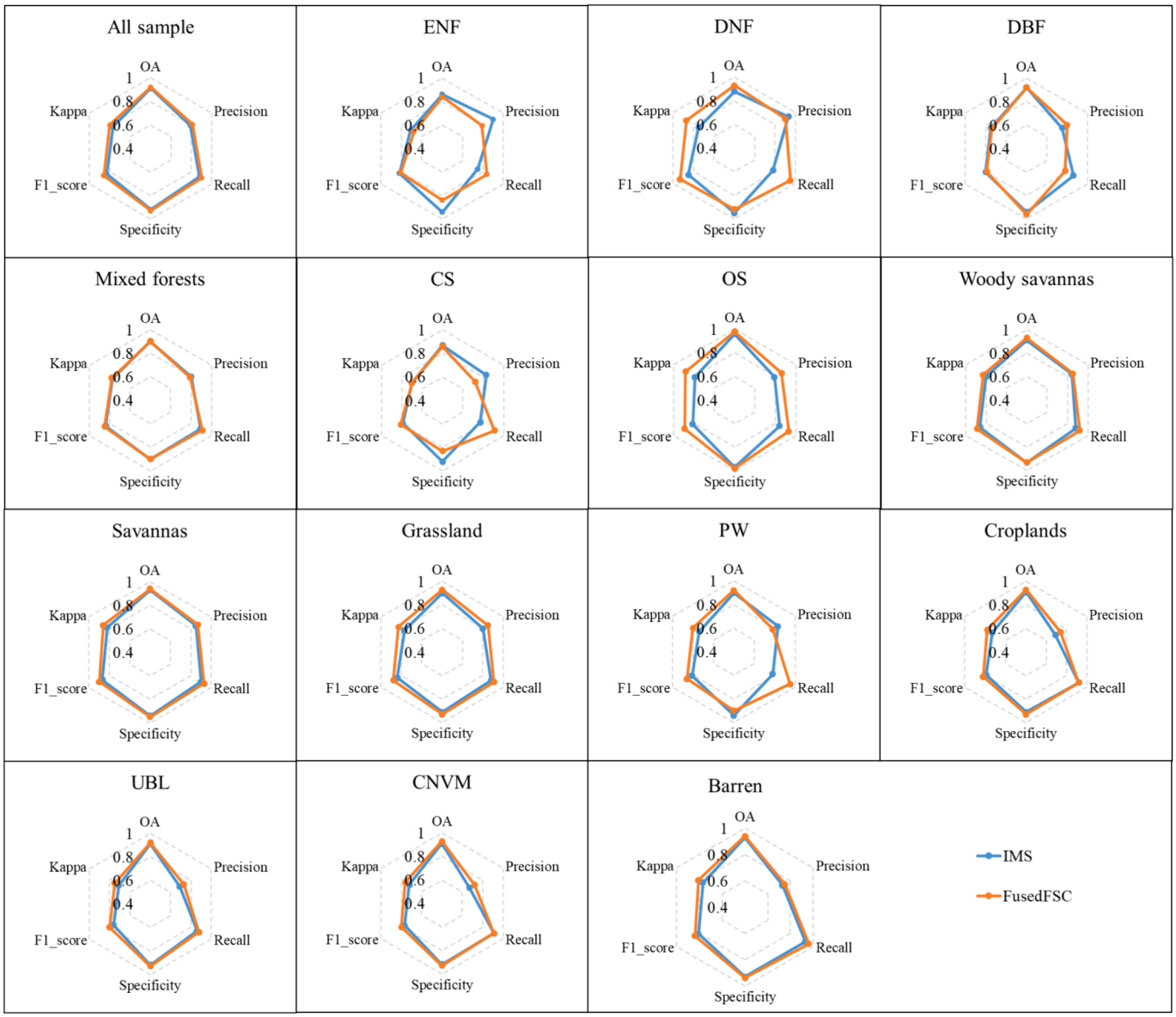

Fig. 9. Overview of accuracy metrics for validating snow cover product (FusedFSC and IMS) using ground snow depth measurements (cf. Table 4). The number of ground snow depth records available for the evergreen broadleaf forests type is limited and, therefore, not displayed in the figure. The abbreviations ENF (evergreen needleleaf forests), NDF (deciduous needleleaf forests), DBF (deciduous broadleaf forests), CS (closed shrublands), OS (open shrublands), PW (permanent wetlands), CNVM (cropland or natural vegetation mosaics), and UBL (urban and built-up lands) are provided for reference.

5. Discussion

5.1. Uncertainties in the input fractional snow cover datasets

To leverage the strengths of both optical-based FSC data, characterized by high spatial resolution, and PM-based FSC data, less susceptible to clouds or atmosphere interference, we developed a data fusion framework that effectively combines these two datasets, resulting in spatially and temporally complete fused FSC estimates. However, some errors have been observed in the fused FSC data (see Sections 4.1 and 4.2), which are potentially attributable to uncertainties in the input FSC data. These uncertainties could potentially arise from 1) the temporal offset of data acquisitions between the PM and MODIS Terra, 2) the variations in reference data used for estimating FSC from PM and MODIS data (Xiao et al., 2022a, 2022b), and 3) the inherent differences in FSC retrieval algorithms employed by the respective satellite sensors. As Chen et al. (2020) highlighted, uncertainties between coarse- and fine-resolution input images can substantially impact the results obtained through the data fusion method.

Specifically, when using optical remote sensing data, the obstruction of tree canopies and the variation in the visible proportion of ground snow under forests with viewing geometry contribute to inconsistencies between observed FSC and actual snow cover in forested areas (Rittger et al., 2020b). To address these limitations, previous studies have undertaken excellent works in analyzing the influence of forest cover and developing canopy correction methods (Kostadinov et al., 2019; Muhuri et al., 2021; Raleigh et al., 2013; Rittger et al., 2020b; Stillinger et al., 2023). Nonetheless, based on previous testing results (Xiao et al., 2022b), the direct application of canopy correction methods may not always yield the desired improvements under all combinations of viewing geometrics and fractional vegetation cover conditions. Therefore, the MODIS_FSC data used in this study excluded all cases exhibiting dense vegetation coverage and large viewing zenith angles (>60°).

Unlike optical-based FSC, passive microwave-based FSC data inversion is influenced by various factors, including forest cover, atmospheric conditions, and soil moisture, all of which can affect microwave

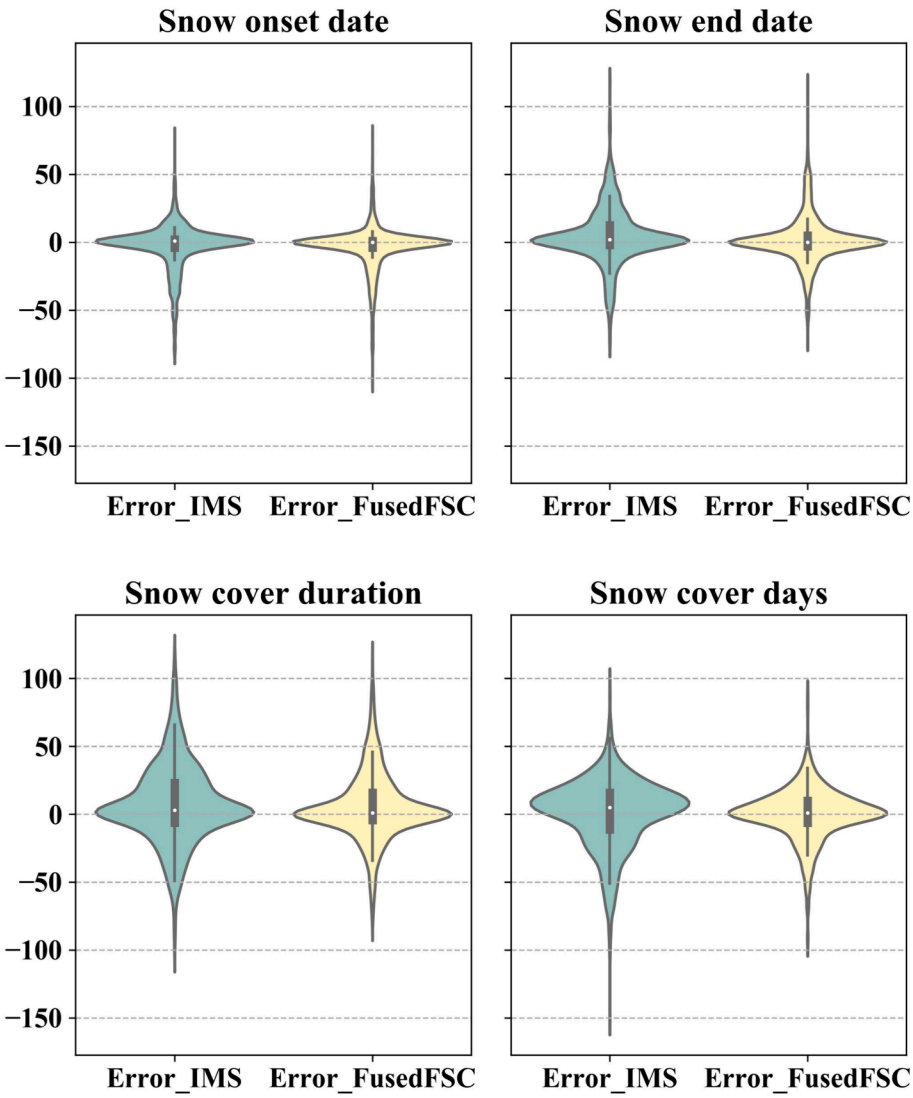

Fig. 10. Violin plots illustrating the error distributions of four snow-cover phenology metrics — snow cover duration, snow onset date, snow end date, and snow cover days — for the fused fractional snow cover data (FusedFSC) and IMS data, compared against snow depth observations from 3,000 sites. The median values of the error distributions are denoted by white dots, while the gray boxes depict the interquartile range. Thin gray lines indicate the 5th and 95th percentiles. The unit of measurement for all metrics is days.

radiation signals (Khazaei et al., 2023; Qiu et al., 2021; Roy et al., 2012; Shahroudi and Rossow, 2014; Xiao et al., 2022a). In PM_FSC data generation, Xiao et al. (2022a) utilized a series of empirical parameters to characterize the propagation and attenuation of microwave radiation (19-, 36-, and 91-GHz) in forested areas through a radiational transfer model, accounting for atmospheric, forest, and topographic influence. However, these empirical parameters possess inherent limitations, resulting in high uncertainties in PM_FSC estimates due to the simplified radiational transfer model (Langlois et al., 2011; Roy et al., 2012). The scattering of microwave radiation caused by variations in soil moisture further complicates the isolation of the snowpack signal (Schattan et al., 2019; Shahroudi and Rossow, 2014). Therefore, Xiao et al. (2022a) developed an FSC retrieval model using passive microwave brightness temperature data, incorporating soil moisture variation information provided by ERA5 reanalysis data.

Apart from the above discussion, the accuracy of FSC estimates derived from optical and passive microwave data both rely on the variations of surface land cover types. Hence, it is crucial for researchers to account for this influence factor when developing a robust retrieval model (Xiao et al., 2022a, 2022b). Additionally, for snow on glaciers, conventional methods for snow cover mapping encounter challenges in distinguishing between snow and ice on glaciers and on land, owing to their similar spectral signature properties (Rastner et al., 2019). However, our previous and current studies have not explicitly considered this distinction between snow and ice on glaciers, potentially resulting in uncertainties in snow cover estimates.

5.2. *Evaluation of the fused fractional snow cover*

This study comprehensively evaluated the fused FSC estimates using a substantial amount of ground-based snow depth data and Landsat images encompassing diverse land cover types. Snow depth measurements from *in-situ* observations are the only source capable of providing daily dynamic observations that serve as a reference benchmark for systematical evaluation. Assessing daily dynamic characteristics is pivotal in evaluating retrieval results for temporally continuous data. In contrast to the previous studies on FSC estimation (Czyzowska-Wisniewski et al., 2015; Dobreva and Klein, 2011; Kuter et al., 2022, 2018), this study introduced an evaluation approach employing snow-cover phenology metrics to assess the daily dynamic characteristics of snow evolution in comparison to snow depth measurements. Our evaluation of the period from September 2015 to May 2016 reveals that FusedFSC

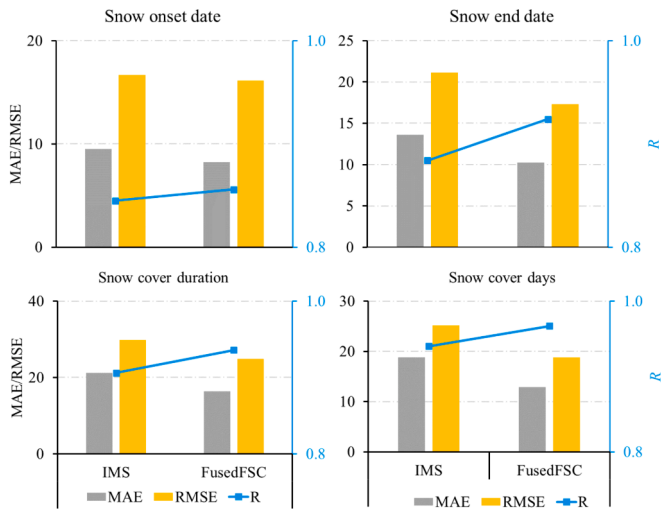

Fig. 11. The accuracy of the four snow-cover phenology metrics (i.e., snow cover duration, snow onset date, snow end date, and snow cover days) in validating the fused fractional snow cover (Fused FSC) and the IMS snow cover data using observations from 3,000 sites. The unit of measurement is days.

outperforms IMS snow cover extent data in terms of overall RMSE and *R* (Figs. 13 and 14), demonstrating its superior ability to depict the daily dynamic characteristics of snow cover. Furthermore, this study deviates from previous studies that directly used IMS snow cover extent data to analyze snow-cover phenology changes (Chen et al., 2015).

The evaluation datasets used faced some limitations owing to the uneven spatial distribution, with the majority of validation data concentrated in the American region and limited data available in Canada. In the context of Landsat reference data, one filtering criterion employed in this study was selecting scenes with cloud cover of less than 1 %, resulting in a significant reduction in the number of available Landsat images. To address these limitations, further research could incorporate additional data from other studies. Vionnet et al. (2021) recently released a comprehensive snow water equivalent dataset spanning a long-time series from 1928 to 2020, combining manual and automated Canadian snowpack observations. Additionally, lidar-based snow depth data have been extensively employed to monitor regional snow cover distribution (Painter et al., 2016) and serve as evaluation reference data (Kostadinov et al., 2019; Stillinger et al., 2023; Xiao et al., 2024). These datasets represent a valuable addition to the snow cover data pool, providing more ground snow cover observations across Canada and various regional basins. Potential options for enhancing the evaluation include allowing for a higher cloud cover percentage (>1%) in Landsat scenes and incorporating some Sentinel-2 data. Nevertheless, it is crucial to implement a transform function to harmonize the reflectance values between Landsat and Sentinel-2 sensors, which can help mitigate uncertainties when using these satellite data sources (Claverie et al., 2018; Zhang et al., 2018).

5.3. Challenges in applying ESTARFM method

The ESTARFM method (Zhu et al., 2010) initially excels at downscaling MODIS surface reflectance and generating high spatiotemporal continuity data. However, it requires spatially complete input data, lead to missing values in the output if any gaps exist. Consequently, previous ESTARFM applications have primarily focused on smaller regions due to the difficulty of acquiring spatially complete imagery across vast areas like North America (Li and Long, 2020; Long et al., 2020; Zhu et al., 2010). Specifically, directly using the unprocessed MODIS_FSC data (data integrity = 38.6 %; Fig. A panel c) with ESTARFM method would result in the data integrity (percentage of pixels with valid values) of the fused FSC data no more than 50 % across North America. That highlights the near practical impossibility of achieving complete cloud-free input FSC data derived from optical satellite images over such a large region using the traditional ESTARFM method. To overcome this limitation, our solution is to integrate a novel spatiotemporal information cube method and the composited ESTARFM method into the data fusion framework (Fig. 2; Section 3.1). This framework mitigates the influence of data gaps and enables the generation of spatiotemporally complete FSC data across North America.

Previous ESTARFM applications typically employed a great time interval (e.g., > 30 days or > 60 days) between reference days (day t_m and day t_n in Eq.6) used for input data selection (Li and Long, 2020; Long et al., 2020, 2019; Zhu et al., 2010). However, FSC data present unique challenges. Unlike continuous and consistent predictor variables studied in previous ESTARFM applications, FSC data can include both zero values (snow-free) and non-zero values (snow-covered), with vastly different interpretations. The inherently dynamic and ephemeral nature of snow cover makes estimating current snow properties using data from months before or after highly unreliable. Rapid snowmelt within a few days can lead to significant errors in FSC estimation if snow-free information is included (Gafurov and Bárdossy 2009; Li et al., 2023). Therefore, established selection methods from previous studies are unsuitable for snow cover applications. Conversely, shallow snow information exhibits a strong correlation with snow cover information on adjacent days (e.g., ± 2 day s or ± 3 day s) (Xiao et al., 2020). To address this, the composited ESTARFM method incorporates data from adjacent ± 2 days within the data fusion framework (Eq. (2) for generating the fused FSC results.

6. Conclusion

This study presents a novel data fusion framework for estimating FSC by effectively overcomes the limitations of traditional satellite based FSC estimation. By leveraging the complementary strengths of coarse- and fine-resolution FSC data, this proposed framework achieves the generations of high-accuracy, spatial completeness, and temporally continuous daily FSC products at a 1-km resolution across vast regions like North America. The thoroughly evaluation demonstrates the framework's superior performance in estimating FSC. The fused FSC data exhibits excellent agreement with independent data (24 scenes of Landsat-based FSC; RMSE 6.8 %-18.9 %). Additionally, the fused FSC data surpasses the mapping capabilities of IMS snow cover extent data, evidenced through OA ranging from 0.84 to 0.98, F1_score ranging from 0.79 to 0.93, and Kappa coefficient ranging from 0.68 to 0.88. Furthermore, the fused FSC data captures daily time-series dynamics of snow cover with greater fidelity compared to the widely used IMS products, as evidenced by snow-cover phenology metrics. These advancements hold significant value for environment applications. In conclusion, the proposed data fusion framework has paved the way for generating high-resolution (1-km), high-accuracy, and spatiotemporally continuous daily FSC data for North America. Beyond North America, the framework's potential extends to global snow cover monitoring. Its all-weather functionality and adaptability to utilize reanalysis data or satellite products make it a versatile tool for generating consistent and comprehensive for global snow cover datasets. These data hold significant value for applications such as hydrological forecasting, climate projections, and various environmental studies. This fosters a deeper understanding of cryosphere processes and their role in the Earth system.

CRediT authorship contribution statement

Xiongxin Xiao: Writing – original draft, Validation, Methodology, Data curation, Conceptualization. **Tao He:** Writing – review & editing, Supervision, Methodology, Funding acquisition, Formal analysis, Conceptualization. **Shuang Liang:** Writing – review & editing. **Shunlin**

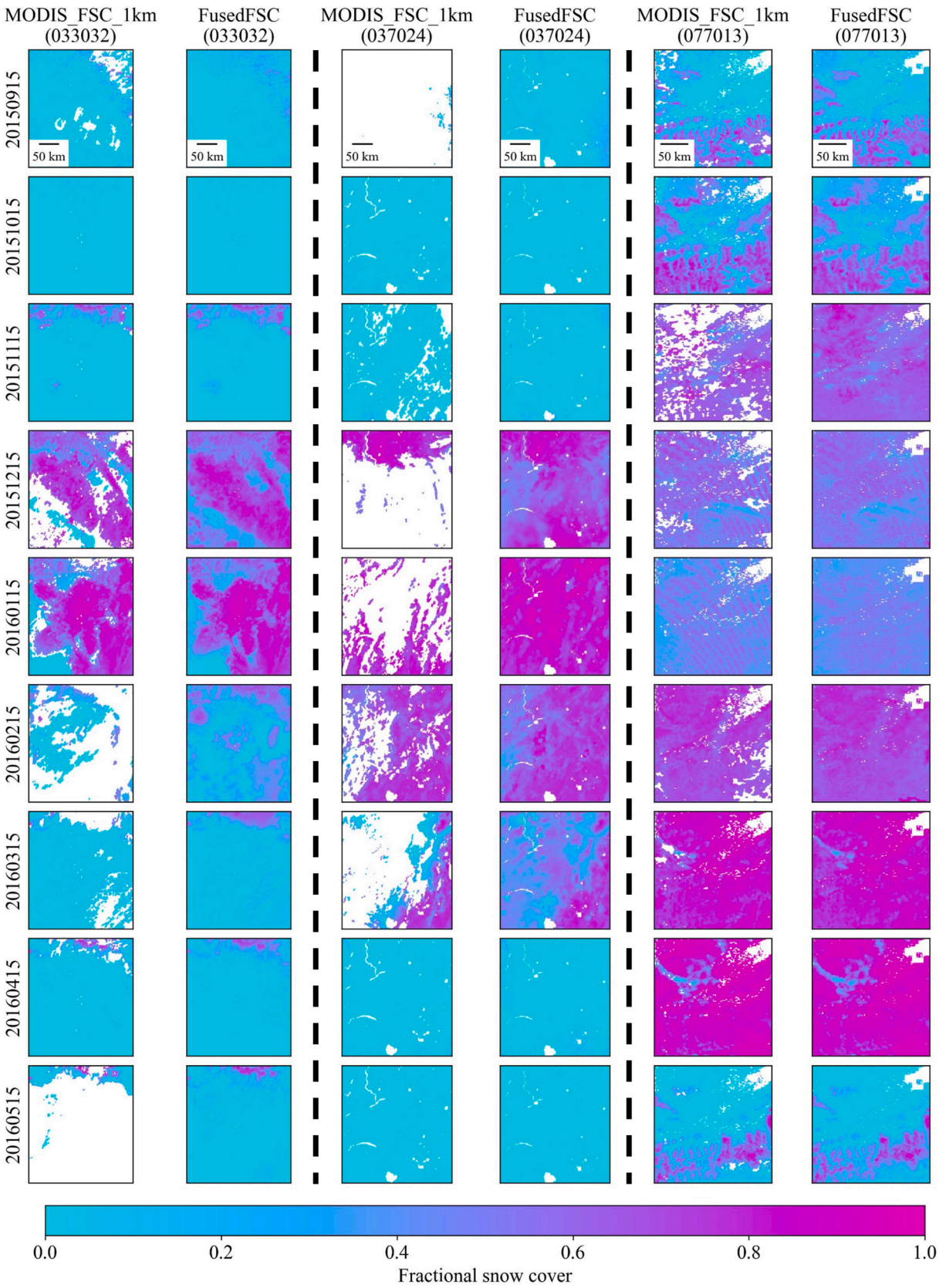

Fig. 12. Comparison of snow cover spatial distribution between MODIS_FSC_1km and FusedFSC results (1 km) on the 15th day of every month from September 2015 to May 2016. The MODIS_FSC_1km for three Landsat scene regions (path/row: 033032, 037024, and 077013) are displayed in the first, third, and fifth columns, respectively. The FusedFSC results are displayed in the second, fourth, and sixth columns. The blank areas represent missing values due to various reasons.

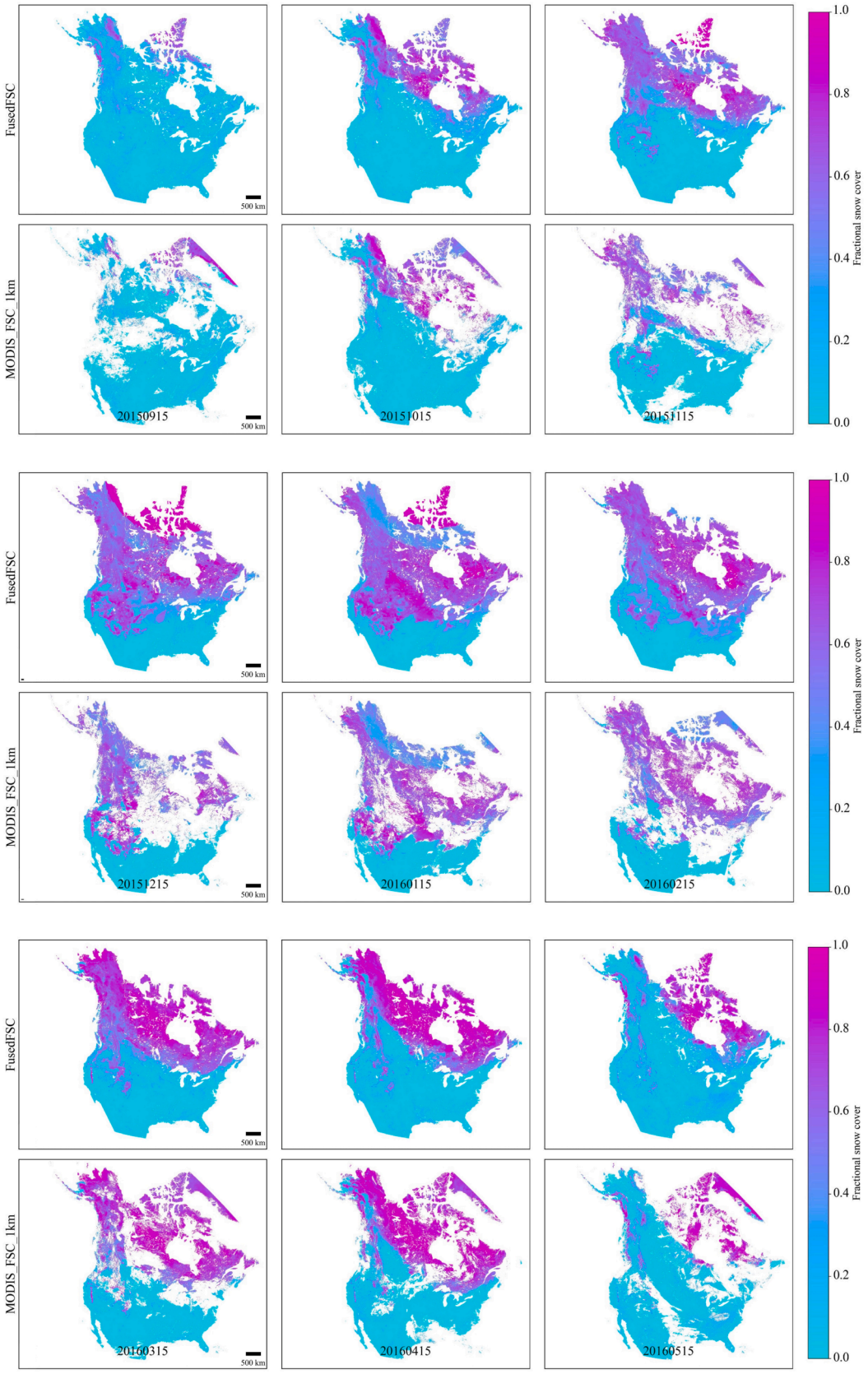

Fig. 13. Spatial distributions of snow cover (1 km) for FusedFSC data and MODIS_FSC_1km data across North America on the 15th day of every month from September 2015 to May 2016. The dates are shown at the bottom of the subplots. The blank areas denote missing values due to various reasons.

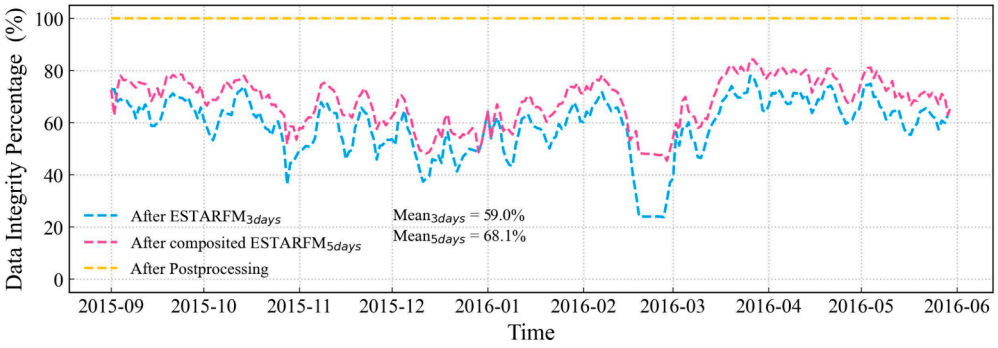

Fig. 14. Data integrity percentage of FusedFSC data after employing three data processing steps. $ESTARFM_{3days}$ denotes the input data from only three consecutive days $(t_p \pm 1)$. $ESTARFM_{5days}$ denotes the input data includes three additional image pairs combinations: $(C_{t_p-1}, F_{t_p-1}, C_{t_p}, C_{t_p+2}, F_{t_p+2})$, $(C_{t_p-2}, F_{t_p-2}, C_{t_p}, C_{t_p+1}, F_{t_p+1})$, and $(C_{t_p-2}, F_{t_p-2}, C_{t_p}, C_{t_p+2}, F_{t_p+2})$.

Liang: Writing – review & editing. **Xinyan Liu:** Writing – review & editing, Validation, Data curation. **Yichuan Ma:** Writing – review & editing, Data curation. **Jun Wan:** Data curation, Methodology, Resources.

Declaration of competing interest

The authors declare that they have no known competing financial interests or personal relationships that could have appeared to influence the work reported in this paper.

Data availability

Data will be made available on request.

Acknowledgments

This study was funded by the Natural Science Foundation of China Grant (42090012), the Natural Science Foundation of Hubei Province Grant (2021CFA082), and the National Key Research and Development Program of China Grant (2020YFA0608704). We appreciate the editorial team and anonymous reviewers for their very constructive comments and suggestions, which help greatly improve the quality of the manuscript.

Appendix

Table A
The information from nine Landsat 8 OLI surface reflectance scenes was used for the evaluation of fractional snow cover estimates.

Landsat scene ID	WRS-path/row	Date Acquired	ID in Figures. and Tables
03303120160106	033/031	January 6, 2016	(a)
03303220160122	033/032	January 12, 2016	(b)
03603520160111	036/035	January 11, 2016	(c)
03702420151201	037/024	December 1, 2015	(d)
07101720160421	071/017	April 21, 2016	(e)
07201620160412	072/016	April 12, 2016	(f)
07701320160415	077/013	April 15, 2016	(g)
07701420160415	077/014	April 15, 2016	(h)
07801320160422	078/013	April 22, 2016	(i)
01602320160506	016/023	May 6, 2016	(1)
02603020151204	026/030	December 4, 2015	(2)
03303220160122	033/032	January 22, 2016	(3)
03903320151113	039/033	November 13, 2015	(4)
04202020160410	042/020	April 10, 2016	(5)
04301420160519	043/014	May 19, 2016	(6)
04302520160401	043/025	April 1, 2016	(7)
04302720151125	043/027	November 25, 2015	(8)
04303320160316	043/033	March 16, 2016	(9)
05202220160331	052/022	March 31, 2016	(10)
06301520160312	063/015	March 12, 2016	(11)
06301720151004	063/017	October 4, 2015	(12)
07101320151012	071/013	October 12, 2015	(13)
07301820160318	073/018	March 18, 2016	(14)
07601320160424	076/013	April 24, 2016	(15)

Table B
FusedFSC Summary of accuracy metrics for the fused fractional snow cover data (FusedFSC) using 15 Landsat scenes FSC data as the reference data.

ID of Landsat scene	*R*	MAE	RMSE
All scenes	0.96	8.3 %	10.2 %
01602320160506	0.81	5.6 %	8.9 %
02603020151204	0.97	2.9 %	6.8 %
03303220160122	0.92	9.7 %	13.6 %
03903320151113	0.96	5.5 %	10.3 %
04202020160410	0.95	8.2 %	11.2 %
04301420160519	0.80	7.7 %	9.4 %
04302520160401	0.91	12.5 %	15.9 %
04302720151125	0.85	14.1 %	18.9 %
04303320160316	0.98	3.4 %	7.4 %
05202220160331	0.90	11.7 %	15.7 %
06301520160312	0.68	12.8 %	14.8 %
06301720151004	0.97	8.0 %	11.9 %
07101320151012	0.91	11.4 %	15.0 %
07301820160318	0.97	8.0 %	9.7 %
07601320160424	0.93	9.7 %	11.5 %

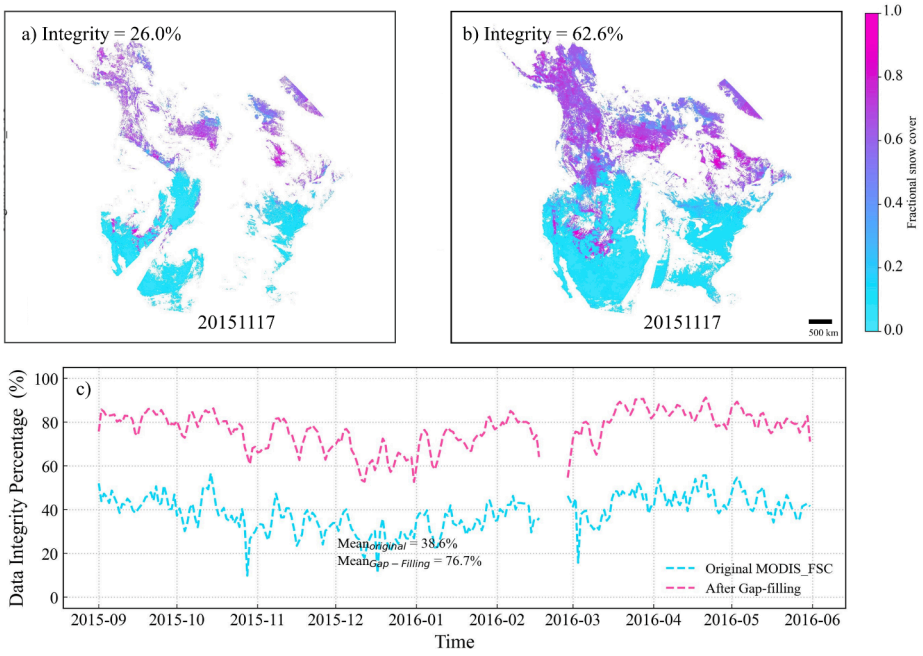

Fig. A. Impact of applying gap-filling on MODIS_FSC Data (500 m). Panels (a) and (b) show original and gap-filled MODIS_FSC data (500 m; November 17, 2015), respectively. Panel (c) displays data integrity percentages before and after gap-filling.

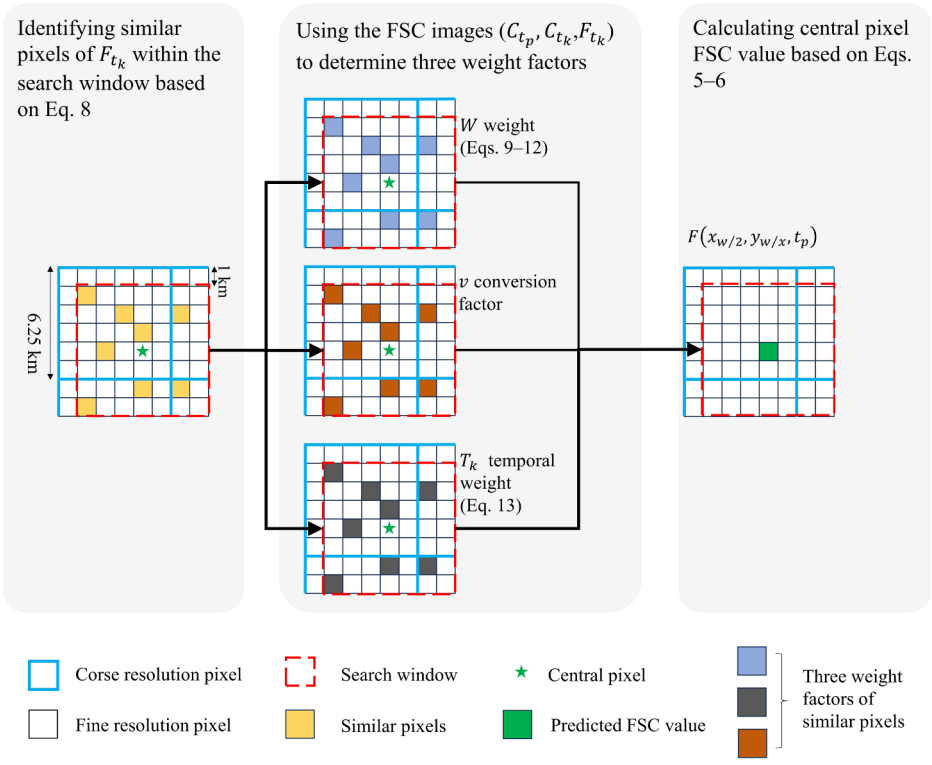

Fig. B. Schematic diagram of the ESTARFM method for predicting fractional snow cover (FSC) value of the central pixel.

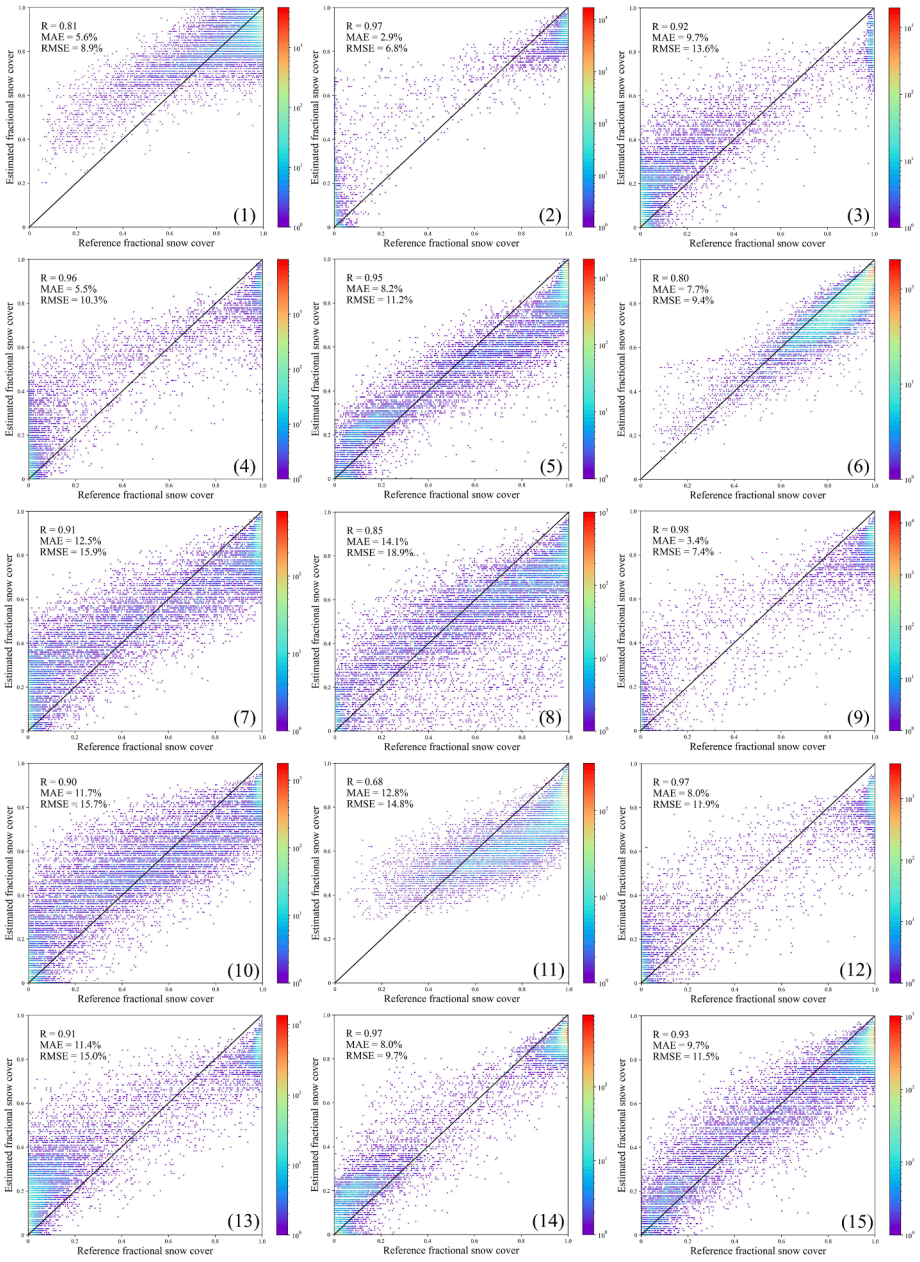

Fig. C. Scatter plot of Landsat reference fractional snow cover (x-axis) versus the fused fractional snow cover (FusedFSC, y-axis) for the nine scenes, with a 1:1 line shown. (1)-(15) denote the ID of Landsat scenes (cf. Table A in the Appendix). FSC is a unitless variable.

References

Barnett, T.P., Adam, J.C., Lettenmaier, D.P., 2005. Potential impacts of a warming climate on water availability in snow-dominated regions. Nature 438, 303–309. https://doi.org/10.1038/nature04141.

Bergeron, J., Royer, A., Turcotte, R., Roy, A., 2014. Snow cover estimation using blended MODIS and AMSR-E data for improved watershed-scale spring streamflow simulation in Quebec, Canada. Hydrol. Process. 28, 4626–4639. https://doi.org/10.1002/hyp.10123.

Berghuijs, W.R., Woods, R.A., Hrachowitz, M., 2014. A precipitation shift from snow towards rain leads to a decrease in streamflow. Nat. Clim. Chang. 4, 583–586. https://doi.org/10.1038/nclimate2246.

Bousbaa, M., Htitiou, A., Boudhar, A., Eljabiri, Y., Elyoussfi, H., Bouamri, H., Ouatiki, H., Chehbouni, A., 2022. High-Resolution Monitoring of the Snow Cover on the Moroccan Atlas through the Spatio-Temporal Fusion of Landsat and Sentinel-2 Images. Remote Sens. 14, 5814. https://doi.org/10.3390/rs14225814.

Brodzik, M.J., Long, D.G., Hardman, M.A., Paget, A., Armstrong, R., 2016. MEaSUREs Calibrated Enhanced-Resolution Passive Microwave Daily EASE-Grid 2.0 Brightness Temperature ESDR, Version 1 NASA National Snow and Ice Data Center Distributed Active Archive Center. NASA National Snow and Ice Data Center Distributed Active Archive Center. doi: 10.5067/MEASURES/CRYOSPHERE/NSIDC-0630.001.

Chen, Y., Cao, R., Chen, J., Zhu, X., Zhou, J., Wang, G., Shen, M., Chen, X., Yang, W., 2020. A new cross-fusion method to automatically determine the optimal input image pairs for NDVI spatiotemporal data fusion. IEEE Trans. Geosci. Remote Sens. 58, 5179–5194. https://doi.org/10.1109/TGRS.2020.2973762.

Chen, C., Lakhankar, T., Romanov, P., Helfrich, S., Powell, A., Khanbilvardi, R., 2012. Validation of NOAA-interactive multisensor snow and Ice Mapping System (IMS) by comparison with ground-based measurements over continental United States. Remote Sens 4, 1134–1145. https://doi.org/10.3390/rs4051134.

Chen, X., Liang, S., Cao, Y., He, T., Wang, D., 2015. Observed contrast changes in snow cover phenology in northern middle and high latitudes from 2001–2014. Sci. Rep. 5, 16820. https://doi.org/10.1038/srep16820.

Claverie, M., Ju, J., Masek, J.G., Dungan, J.L., Vermote, E.F., Roger, J.C., Skakun, S.V., Justice, C., 2018. The Harmonized Landsat and Sentinel-2 surface reflectance data set. Remote Sens. Environ. 219, 145–161. https://doi.org/10.1016/j.rse.2018.09.002.

Cristea, N.C., Breckheimer, I., Raleigh, M.S., HilleRisLambers, J., Lundquist, J.D., 2017. An evaluation of terrain-based downscaling of fractional snow covered area data sets based on LiDAR-derived snow data and orthoimagery. Water Resour. Res. 53, 6802–6820. https://doi.org/10.1002/2017WR020799.

Czyzowska-Wisniewski, E.H., van Leeuwen, W.J.D., Hirschboeck, K.K., Marsh, S.E., Wisniewski, W.T., 2015. Fractional snow cover estimation in complex alpine-forested environments using an artificial neural network. Remote Sens. Environ. 156, 403–417. https://doi.org/10.1016/j.rse.2014.09.026.

Deng, J., Huang, X., Feng, Q., Ma, X., Liang, T., 2015. Toward improved daily cloud-free fractional snow cover mapping with multi-source remote sensing data in China. Remote Sens 7, 6986–7006. https://doi.org/10.3390/rs70606986.

Dietz, A.J., Kuenzer, C., Gessner, U., Dech, S., 2012. Remote sensing of snow - a review of available methods. Int. J. Remote Sens. 33, 4094–4134. https://doi.org/10.1080/01431161.2011.640964.

Dobreva, I.D., Klein, A.G., 2011. Fractional snow cover mapping through artificial neural network analysis of MODIS surface reflectance. Remote Sens. Environ. 115, 3355–3366. https://doi.org/10.1016/j.rse.2011.07.018.

Dozier, J., 1989. Spectral signature of alpine snow cover from the landsat thematic mapper. Remote Sens. Environ. 28, 9–22. https://doi.org/10.1016/0034-4257(89)90101-6.

Dozier, J., Painter, T.H., Rittger, K., Frew, J.E., 2008. Time-space continuity of daily maps of fractional snow cover and albedo from MODIS. Adv. Water Resour. 31, 1515–1526. https://doi.org/10.1016/j.advwatres.2008.08.011.

Foster, J.L., Hall, D.K., Eylander, J.B., Riggs, G.A., Nghiem, S.V., Tedesco, M., Kim, E., Montesano, P.M., Kelly, R.E.J., Casey, K.A., Choudhury, B., 2011. A blended global snow product using visible, passive microwave and scatterometer satellite data. Int. J. Remote Sens. 32, 1371–1395. https://doi.org/10.1080/01431160903548013.

Gafurov, A., Bárdossy, A., 2009. Cloud removal methodology from MODIS snow cover product. Hydrol. Earth Syst. Sci. 13, 1361–1373. https://doi.org/10.5194/hess-13-1361-2009.

Gao, M., Gu, X., Liu, Y., Zhan, Y., Wei, X., Yu, H., Liang, M., Weng, C., Ding, Y., 2022. An Improved Spatiotemporal Data Fusion Method for Snow-Covered Mountain Areas Using Snow Index and Elevation Information. Sensors 22, 8524. https://doi.org/10.3390/s22218524.

Gao, F., Masek, J., Schwaller, M., Hall, F., 2006. On the blending of the Landsat and MODIS surface reflectance: Predicting daily Landsat surface reflectance. IEEE Trans. Geosci. Remote Sens. 44, 2207–2218. https://doi.org/10.1109/TGRS.2006.872081.

Gao, Y., Xie, H., Lu, N., Yao, T., Liang, T., 2010. Toward advanced daily cloud-free snow cover and snow water equivalent products from Terra-Aqua MODIS and Aqua AMSR-E measurements. J. Hydrol. 385, 23–35. https://doi.org/10.1016/j.jhydrol.2010.01.022.

Gascoin, S., Grizonnet, M., Bouchet, M., Salgues, G., Hagolle, O., 2019. Theia Snow collection: High-resolution operational snow cover maps from Sentinel-2 and Landsat-8 data. Earth Syst. Sci. Data 11, 493–514. https://doi.org/10.5194/essd-11-493-2019.

Girona-Mata, M., Miles, E.S., Ragettli, S., Pellicciotti, F., 2019. High-Resolution Snowline Delineation From Landsat Imagery to Infer Snow Cover Controls in a Himalayan Catchment. Water Resour. Res. 55, 6754–6772. https://doi.org/10.1029/2019WR024935.

Grody, N.C., Basist, A.N., 1996. Global identification of snow cover using SSM/I measurements. IEEE Trans. Geosci. Remote Sens. https://doi.org/10.1109/36.481908.

Guglielmetti, M., Schwank, M., Mätzler, C., Oberdörster, C., Vanderborght, J., Flühler, H., 2007. Measured microwave radiative transfer properties of a deciduous forest canopy. Remote Sens. Environ. 109, 523–532. https://doi.org/10.1016/j.rse.2007.02.003.

Hall, D.K., Riggs, G.A., 2007. Accuracy assessment of the MODIS snow products. Hydrol. Process. https://doi.org/10.1002/hyp.6715.

Hall, D.K., Riggs, G.A., Salomonson, V.V., 1995. Development of methods for mapping global snow cover using moderate resolution imaging spectroradiometer data. Remote Sens. Environ. https://doi.org/10.1016/0034-4257(95)00137-P.

Hao, X., Huang, G., Che, T., Ji, W., Sun, X., Zhao, Q., Zhao, H., Wang, J., Li, H., Yang, Q., 2021. The NIEER AVHRR snow cover extent product over China - A long-term daily snow record for regional climate research. Earth Syst. Sci. Data 13, 4711–4726. https://doi.org/10.5194/essd-13-4711-2021.

Hedrick, A.R., Marks, D., Havens, S., Robertson, M., Johnson, M., Sandusky, M., Marshall, H.P., Kormos, P.R., Bormann, K.J., Painter, T.H., 2018. Direct Insertion of NASA Airborne Snow Observatory-Derived Snow Depth Time Series Into the iSnobal Energy Balance Snow Model. Water Resour. Res. 54, 8045–8063. https://doi.org/10.1029/2018WR023190.

Helfrich, S.R., McNamara, D., Ramsay, B.H., Baldwin, T., Kasheta, T., 2007. Enhancements to, and forthcoming developments in the Interactive Multisensor Snow and Ice Mapping System (IMS). Hydrol. Process. 21, 1576–1586. https://doi.org/10.1002/hyp.6720.

Huang, X., Deng, J., Ma, X., Wang, Y., Feng, Q., Hao, X., Liang, T., 2016. Spatiotemporal dynamics of snow cover based on multi-source remote sensing data in China. Cryosphere 10, 2453–2463. https://doi.org/10.5194/tc-10-2453-2016.

Huang, Y., Liu, H., Yu, B., Wu, J., Kang, E.L., Xu, M., Wang, S., Klein, A., Chen, Y., 2018. Improving MODIS snow products with a HMRF-based spatio-temporal modeling technique in the Upper Rio Grande Basin. Remote Sens. Environ. 204, 568–582. https://doi.org/10.1016/j.rse.2017.10.001.

Jing, Y., Li, X., Shen, H., 2022. STAR NDSI collection: a cloud-free MODIS NDSI dataset (2001–2020) for China. Earth Syst. Sci. Data 14, 3137–3156. https://doi.org/10.5194/essd-14-3137-2022.

Khazaei, M., Hamzeh, S., Samani, N.N., Muhuri, A., Goïta, K., Weng, Q., 2023. A web-based system for satellite-based high-resolution global soil moisture maps. Comput. Geosci. 170, 105250 https://doi.org/10.1016/J.CAGEO.2022.105250.

Klein, G., Vitasse, Y., Rixen, C., Marty, C., Rebetez, M., 2016. Shorter snow cover duration since 1970 in the swiss alps due to earlier snowmelt more than to later snow onset. Clim. Change 139, 637–649. https://doi.org/10.1007/s10584-016-1806-y.

Kong, J., Ryu, Y., Huang, Y., Dechant, B., Houborg, R., Guan, K., Zhu, X., 2021. Evaluation of four image fusion NDVI products against in-situ spectral-measurements over a heterogeneous rice paddy landscape. Agric. For. Meteorol. 297, 108255 https://doi.org/10.1016/j.agrformet.2020.108255.

Kostadinov, T.S., Schumer, R., Hausner, M., Bormann, K.J., Gaffney, R., McGwire, K., Painter, T.H., Tyler, S., Harpold, A.A., 2019. Watershed-scale mapping of fractional snow cover under conifer forest canopy using lidar. Remote Sens. Environ. 222, 34–49. https://doi.org/10.1016/j.rse.2018.11.037.

Kuter, S., Akyurek, Z., Weber, G.-W., 2018. Retrieval of fractional snow covered area from MODIS data by multivariate adaptive regression splines. Remote Sens. Environ. 205, 236–252. https://doi.org/10.1016/j.rse.2017.11.021.

Kuter, S., Bolat, K., Akyurek, Z., 2022. A machine learning-based accuracy enhancement on EUMETSAT H-SAF H35 effective snow-covered area product. Remote Sens. Environ. 272, 112947 https://doi.org/10.1016/j.rse.2022.112947.

Langlois, A., Royer, A., Dupont, F., Roy, A., Goita, K., Picard, G., 2011. Improved corrections of forest effects on passive microwave satellite remote sensing of snow over boreal and subarctic regions. IEEE Trans. Geosci. Remote Sens. 49, 3824–3837. https://doi.org/10.1109/TGRS.2011.2138145.

Lettenmaier, D.P., Alsdorf, D., Dozier, J., Huffman, G.J., Pan, M., Wood, E.F., 2015. Inroads of remote sensing into hydrologic science during the WRR era. Water Resour. Res. 51, 7309–7342. https://doi.org/10.1111/j.1752-1688.1969.tb04897.x.

Li, D., Lu, X., Walling, D.E., Zhang, T., Steiner, J.F., Wasson, R.J., Harrison, S., Nepal, S., Nie, Y., Immerzeel, W.W., Shugar, D.H., Koppes, M., Lane, S., Zeng, Z., Sun, X., Yegorov, A., Bolch, T., 2022. High Mountain Asia hydropower systems threatened by climate-driven landscape instability. Nature Geoscience 2022 15:7 15, 520–530. doi: 10.1038/s41561-022-00953-y.

Li, X., Long, D., 2020. An improvement in accuracy and spatiotemporal continuity of the MODIS precipitable water vapor product based on a data fusion approach. Remote Sens. Environ. 248, 111966 https://doi.org/10.1016/j.rse.2020.111966.

Li, Y., Wu, H., Chen, H., Zhu, X., 2023. A Robust Framework for Resolution Enhancement of Land Surface Temperature by Combining Spatial Downscaling and Spatiotemporal Fusion Methods. IEEE Trans. Geosci. Remote Sens. 61, 1–14. https://doi.org/10.1109/TGRS.2023.3283614.

Li, X., Zhang, L., Weihermüller, L., Jiang, L., Vereecken, H., 2014. Measurement and simulation of topographic effects on passive microwave remote sensing over mountain areas: A case study from the tibetan plateau. IEEE Trans. Geosci. Remote Sens. 52, 1489–1501. https://doi.org/10.1109/TGRS.2013.2251887.

Liang, T., Zhang, X., Xie, H., Wu, C., Feng, Q., Huang, X., Chen, Q., 2008. Toward improved daily snow cover mapping with advanced combination of MODIS and AMSR-E measurements. Remote Sens. Environ. 112, 3750–3761. https://doi.org/10.1016/j.rse.2008.05.010.

Liu, X., Jiang, L., Wu, S., Hao, S., Wang, G., Yang, J., 2018. Assessment of methods for passive microwave snow cover mapping using FY-3C/MWRI data in China. Remote Sens 10, 524. https://doi.org/10.3390/rs10040524.

Liu, J., Melloh, R.A., Woodcock, C.E., Davis, R.E., Painter, T.H., McKenzie, C., 2008. Modeling the view angle dependence of gap fractions in forest canopies: Implications for mapping fractional snow cover using optical remote sensing. J. Hydrometeorol. 9, 1005–1019. https://doi.org/10.1175/2008JHM866.1.

Long, D., Bai, L., Yan, L., Zhang, C., Yang, W., Lei, H., Quan, J., Meng, X., Shi, C., 2019. Generation of spatially complete and daily continuous surface soil moisture of high spatial resolution. Remote Sens. Environ. 233, 111364 https://doi.org/10.1016/j.rse.2019.111364.

Long, D., Yan, L., Bai, L., Zhang, C., Li, X., Lei, H., Yang, H., Tian, F., Zeng, C., Meng, X., Shi, C., 2020. Generation of MODIS-like land surface temperatures under all-weather conditions based on a data fusion approach. Remote Sens. Environ. 246, 111863 https://doi.org/10.1016/j.rse.2020.111863.

López-Moreno, J.I., Pomeroy, J.W., Alonso-González, E., Morán-Tejeda, E., Revuelto, J., 2020. Decoupling of warming mountain snowpacks from hydrological regimes. Environ. Res. Lett. 15, 114006 https://doi.org/10.1088/1748-9326/abb55f.

Maurer, E.P., Rhoads, J.D., Dubayah, R.O., Lettenmaier, D.P., 2003. Evaluation of the snow-covered area data product from MODIS. Hydrol. Process. 17, 59–71. https://doi.org/10.1002/hyp.1193.

Menne, M.J., Durre, I., Korzeniewski, B., McNeal, S., Thomas, K., Yin, X., Anthony, S., Ray, R., Vose, R.S., Gleason, B.E., Houston, T.G., 2012. Global Historical Climatology Network. NOAA Climatic Data Center. https://doi.org/10.7289/V5D21VHZ.

Muhuri, A., Gascoin, S., Menzel, L., Kostadinov, T.S., Harpold, A.A., Sanmiguel-Vallelado, A., Lopez-Moreno, J.I., 2021. Performance Assessment of Optical Satellite-Based Operational Snow Cover Monitoring Algorithms in Forested Landscapes. IEEE J. Sel. Top. Appl. Earth Obs. Remote Sens. 14, 7159–7178. https://doi.org/10.1109/JSTARS.2021.3089655.

Musselman, K.N., Addor, N., Vano, J.A., Molotch, N.P., 2021. Winter melt trends portend widespread declines in snow water resources. Nat. Clim. Chang. 11, 418–424. https://doi.org/10.1038/s41558-021-01014-9.

Nietupski, T.C., Kennedy, R.E., Temesgen, H., Kerns, B.K., 2021. Spatiotemporal image fusion in Google Earth Engine for annual estimates of land surface phenology in a heterogenous landscape. Int. J. Appl. Earth Obs. Geoinf. 99, 102323 https://doi.org/10.1016/j.jag.2021.102323.

Painter, T.H., Rittger, K., McKenzie, C., Slaughter, P., Davis, R.E., Dozier, J., 2009. Retrieval of subpixel snow covered area, grain size, and albedo from MODIS. Remote Sens. Environ. 113, 868–879. https://doi.org/10.1016/j.rse.2009.01.001.

Painter, T.H., Berisford, D.F., Boardman, J.W., Bormann, K.J., Deems, J.S., Gehrke, F., Hedrick, A., Joyce, M., Laidlaw, R., Marks, D., Mattmann, C., McGurk, B., Ramirez, P., Richardson, M., Skiles, S.M.K., Seidel, F.C., Winstral, A., 2016. The Airborne Snow Observatory: Fusion of scanning lidar, imaging spectrometer, and

physically-based modeling for mapping snow water equivalent and snow albedo. Remote Sens. Environ. 184, 139–152. https://doi.org/10.1016/j.rse.2016.06.018.
Parajka, J., Holko, L., Kostka, Z., Blöschl, G., 2012. MODIS snow cover mapping accuracy in a small mountain catchment - Comparison between open and forest sites. Hydrol. Earth Syst. Sci. 16, 2365–2377. https://doi.org/10.5194/hess-16-2365-2012.
Qin, Y., Abatzoglou, J.T., Siebert, S., Huning, L.S., AghaKouchak, A., Mankin, J.S., Hong, C., Tong, D., Davis, S.J., Mueller, N.D., 2020. Agricultural risks from changing snowmelt. Nat. Clim. Chang. 10, 459–465. https://doi.org/10.1038/s41558-020-0746-8.
Qiu, Y., Shi, L., Lemmetyinen, J., Shi, J., Wang, R.Y., 2021. Atmospheric Correction to Passive Microwave Brightness Temperature in Snow Cover Mapping Over China. IEEE Trans. Geosci. Remote Sens. 59, 6482–6495. https://doi.org/10.1109/TGRS.2020.3031837.
Qiu, S., Zhu, Z., He, B., 2019. Fmask 4.0: Improved cloud and cloud shadow detection in Landsats 4–8 and Sentinel-2 imagery. Remote Sens. Environ. 231, 111205 https://doi.org/10.1016/j.rse.2019.05.024.
Raleigh, M.S., Rittger, K., Moore, C.E., Henn, B., Lutz, J.A., Lundquist, J.D., 2013. Ground-based testing of MODIS fractional snow cover in subalpine meadows and forests of the Sierra Nevada. Remote Sens. Environ. 128, 44–57. https://doi.org/10.1016/j.rse.2012.09.016.
Rastner, P., Prinz, R., Notarnicola, C., Nicholson, L., Sailer, R., Schwaizer, G., Paul, F., 2019. On the automated mapping of snow cover on glaciers and calculation of snow line altitudes from multi-temporal Landsat data. Remote Sens 11, 1–24. https://doi.org/10.3390/rs11121410.
Riggs, G.A., Hall, D.K., Román, M.O., 2017. Overview of NASA's MODIS and Visible Infrared Imaging Radiometer Suite (VIIRS) snow-cover Earth System Data Records. Earth Syst. Sci. Data. https://doi.org/10.5194/essd-9-765-2017.
Rittger, K., Bair, E.H., Kahl, A., Dozier, J., 2016. Spatial estimates of snow water equivalent from reconstruction. Adv. Water Resour. 94, 345–363. https://doi.org/10.1016/j.advwatres.2016.05.015.
Rittger, K., Bormann, K.J., Bair, E.H., Dozier, J., Painter, T.H., 2020a. Evaluation of VIIRS and MODIS snow covered fraction in High Mountain Asia using Landsat 8. Frontiers in Remote Sensing 2, 1–15. https://doi.org/10.3389/frsen.2021.647154.
Rittger, K., Raleigh, M.S., Dozier, J., Hill, A.F., Lutz, J.A., Painter, T.H., 2020b. Canopy Adjustment and Improved Cloud Detection for Remotely Sensed Snow Cover Mapping. Water Resour. Res. 56, 1–20. https://doi.org/10.1029/2019WR024914.
Rittger, K., Krock, M., Kleiber, W., Bair, E.H., Brodzik, M.J., Stephenson, T.R., Rajagopalan, B., Bormann, K.J., Painter, T.H., 2021. Multi-sensor fusion using random forests for daily fractional snow cover at 30 m. Remote Sens. Environ. 264, 112608 https://doi.org/10.1016/j.rse.2021.112608.
Romanov, P., 2017. Global Multisensor Automated satellite-based Snow and Ice Mapping System (GMASI) for cryosphere monitoring. Remote Sens. Environ. 196, 42–55. https://doi.org/10.1016/j.rse.2017.04.023.
Romanov, P., Gutman, G., Csiszar, I., 2000. Automated monitoring of snow cover over North America with multispectral satellite data. J. Appl. Meteorol. 39, 1866–1880. https://doi.org/10.1175/1520-0450(2000)039<1866:AMOSCO>2.0.CO;2.
Roy, A., Royer, A., Wigneron, J.P., Langlois, A., Bergeron, J., Cliche, P., 2012. A simple parameterization for a boreal forest radiative transfer model at microwave frequencies. Remote Sens. Environ. 124, 371–383. https://doi.org/10.1016/j.rse.2012.05.020.
Savoie, M.H., Armstrong, R.L., Brodzik, M.J., Wang, J.R., 2009. Atmospheric corrections for improved satellite passive microwave snow cover retrievals over the Tibet Plateau. Remote Sens. Environ. 113, 2661–2669. https://doi.org/10.1016/j.rse.2009.08.006.
Schattan, P., Köhli, M., Schrön, M., Baroni, G., Oswald, S.E., 2019. Sensing Area-Average Snow Water Equivalent with Cosmic-Ray Neutrons: The Influence of Fractional Snow Cover. Water Resour. Res. 55, 10796–10812. https://doi.org/10.1029/2019WR025647.
Shahroudi, N., Rossow, W., 2014. Using land surface microwave emissivities to isolate the signature of snow on different surface types. Remote Sens. Environ. 152, 638–653. https://doi.org/10.1016/j.rse.2014.07.008.
Shugar, D.H., Jacquemart, M., Shean, D., Bhushan, S., Upadhyay, K., Sattar, A., Schwanghart, W., McBride, S., de Vries, M.V.W., Mergili, M., Emmer, A., Deschamps-Berger, C., McDonnell, M., Bhambri, R., Allen, S., Berthier, E., Carrivick, J.L., Clague, J.J., Dokukin, M., Dunning, S.A., Frey, H., Gascoin, S., Haritashya, U.K., Huggel, C., Kääb, A., Kargel, J.S., Kavanaugh, J.L., Lacroix, P., Petley, D., Rupper, S., Azam, M.F., Cook, S.J., Dimri, A.P., Eriksson, M., Farinotti, D., Fiddes, J., Gnyawali, K.R., Harrison, S., Jha, M., Koppes, M., Kumar, A., Leinss, S., Majeed, U., Mal, S., Muhuri, A., Noetzli, J., Paul, F., Rashid, I., Sain, K., Steiner, J., Ugalde, F., Watson, C.S., Westoby, M.J., 2021. A massive rock and ice avalanche caused the 2021 disaster at Chamoli. Indian Himalaya. Science 1979 (373), 300–306. https://doi.org/10.1126/science.abh4455.
Stillinger, T., Rittger, K., Raleigh, M.S., Michell, A., Davis, R.E., Bair, E.H., 2023. Landsat, MODIS, and VIIRS snow cover mapping algorithm performance as validated by airborne lidar datasets. Cryosphere 17, 567–590. https://doi.org/10.5194/tc-17-567-2023.
Sturm, M., 2015. White water: Fifty years of snow research in WRR and the outlook for the future. Water Resour. Res. 51, 4948–4965. https://doi.org/10.1002/2015WR017242.
Vionnet, V., Mortimer, C., Brady, M., Arnal, L., Brown, R., 2021. Canadian historical Snow Water Equivalent dataset (CanSWE, 1928–2020). Earth Syst. Sci. Data 13, 4603–4619. https://doi.org/10.5194/essd-13-4603-2021.
Wang, G., Jiang, L., Hao, S., Liu, X., Yang, J., Cui, H., 2018. Cloud-Free Fractional Snow Cover Estimation from Blended MODIS and FY-2 VISSR Measurements, in: IGARSS 2018 - 2018 IEEE International Geoscience and Remote Sensing Symposium. IEEE, pp. 5191–5194. doi: 10.1109/IGARSS.2018.8517593.
Wang, G., Jiang, L., Shi, J., Su, X., 2021. A Universal Ratio Snow Index for Fractional Snow Cover Estimation. IEEE Geosci. Remote Sens. Lett. 18, 721–725. https://doi.org/10.1109/LGRS.2020.2982053.
Wulder, M.A., Masek, J.G., Cohen, W.B., Loveland, T.R., Woodcock, C.E., 2012. Opening the archive: How free data has enabled the science and monitoring promise of Landsat. Remote Sens. Environ. 122, 2–10. https://doi.org/10.1016/j.rse.2012.01.010.
Xiao, X., Liang, S., 2024. Assessment of snow cover mapping algorithms from Landsat surface reflectance data and application to automated snowline delineation. Remote Sens. Environ. 307, 114163 https://doi.org/10.1016/j.rse.2024.114163.
Xiao, X., Zhang, T., Zhong, X., Shao, W., Li, X., 2018. Support vector regression snow-depth retrieval algorithm using passive microwave remote sensing data. Remote Sens. Environ. 210, 48–64. https://doi.org/10.1016/j.rse.2018.03.008.
Xiao, X., Zhang, T., Zhong, X., Li, X., 2020. Spatiotemporal Variation of Snow Depth in the Northern Hemisphere from 1992 to 2016. Remote Sens. 12, 2728. https://doi.org/10.3390/rs12172728.
Xiao, X., Liang, S., He, T., Wu, D., Pei, C., Gong, J., 2021. Estimating fractional snow cover from passive microwave brightness temperature data using MODIS snow cover product over North America. Cryosphere 15, 835–861. https://doi.org/10.5194/tc-15-835-2021.
Xiao, X., He, T., Liang, S., Zhao, T., 2022a. Improving Fractional Snow Cover Retrieval From Passive Microwave Data Using a Radiative Transfer Model and Machine Learning Method. IEEE Trans. Geosci. Remote Sens. 60, 1–15. https://doi.org/10.1109/TGRS.2021.3128524.
Xiao, X., He, T., Liang, S., Liu, X., Ma, Y., Liang, S., Chen, X., 2022b. Estimating fractional snow cover in vegetated environments using MODIS surface reflectance data. Int. J. Appl. Earth Obs. Geoinf. 114, 103030 https://doi.org/10.1016/j.jag.2022.103030.
Xin, Q., Woodcock, C.E., Liu, J., Tan, B., Melloh, R.A., Davis, R.E., 2012. View angle effects on MODIS snow mapping in forests. Remote Sens. Environ. 118, 50–59. https://doi.org/10.1016/j.rse.2011.10.029.
Xing, D., Hou, J., Huang, C., Zhang, W., 2022. Spatiotemporal Reconstruction of MODIS Normalized Difference Snow Index Products Using U-Net with Partial Convolutions. Remote Sens 14, 1795. https://doi.org/10.3390/rs14081795.
Yang, J., Jiang, L., Shi, J., Wu, S., Sun, R., Yang, H., 2014. Monitoring snow cover using Chinese meteorological satellite data over China. Remote Sens. Environ. 143, 192–203. https://doi.org/10.1016/j.rse.2013.12.022.
Yu, Y., Renzullo, L.J., McVicar, T.R., Malone, B.P., Tian, S., 2023. Generating daily 100 m resolution land surface temperature estimates continentally using an unbiased spatiotemporal fusion approach. Remote Sens. Environ. 297 https://doi.org/10.1016/j.rse.2023.113784.
Zhang, H.K., Roy, D.P., Yan, L., Li, Z., Huang, H., Vermote, E., Skakun, S., Roger, J.C., 2018. Characterization of Sentinel-2A and Landsat-8 top of atmosphere, surface, and nadir BRDF adjusted reflectance and NDVI differences. Remote Sens. Environ. 215, 482–494. https://doi.org/10.1016/J.RSE.2018.04.031.
Zhou, H., Aizen, E., Aizen, V., 2013. Deriving long term snow cover extent dataset from AVHRR and MODIS data: Central Asia case study. Remote Sens. Environ. 136, 146–162. https://doi.org/10.1016/j.rse.2013.04.015.
Zhu, X., Chen, J., Gao, F., Chen, X., Masek, J.G., 2010. An enhanced spatial and temporal adaptive reflectance fusion model for complex heterogeneous regions. Remote Sens. Environ. 114, 2610–2623. https://doi.org/10.1016/j.rse.2010.05.032.